Karlsruhe Institute of Technology

Department of Physics
Institute of Experimental Particle Physics (ETP)

Sensitivity Studies of the Scintillating Active Transverse Energy Filter for the KATRIN Experiment

Master's Thesis by

Nathanael Simon Gutknecht

at the Institute of Experimental Particle Physics (ETP)

Reviewer:	Prof. Dr. Guido Drexlin
Second Reviewer:	Prof. Dr. Kathrin Valerius
Advisors:	Dr. Anton Huber
	Dr. Dominic Hinz
	M. Sc. Joscha Lauer

Submission Date: 21st November 2023

Erklärung zur Selbstständigkeit

Ich versichere, dass ich diese Arbeit selbstständig verfasst habe und keine anderen als die angegebenen Quellen und Hilfsmittel benutzt habe, die wörtlich oder inhaltlich übernommenen Stellen als solche kenntlich gemacht und die Satzung des KIT zur Sicherung guter wissenschaftlicher Praxis in der gültigen Fassung vom 30.09.2021 beachtet habe.

Karlsruhe, den 21.11.2023, Nathanael Simon Gutknecht

Updated version for publication on the website. Includes some minor changes.

Contents

List of Figures

List of Tables

Abstract

The **Ka**rlsruhe **Tri**tium **N**eutrino (KATRIN) experiment is a setup for a direct neutrino mass measurement with sub-electronvolt precision. For this, the energy of β-electrons emitted in the decay of tritium is measured with high accuracy using an electrostatic filter in combination with magnetic adiabatic collimation (MAC-E-filter).

At the moment, the sensitivity of the experiment is mainly limited by statistical uncertainty stemming from a higher than expected background rate in the experiment. The currently favored hypothesis for this additional background contribution involves the ionization of Rydberg atoms by black body radiation in the main spectrometer. Such a background would show up at the detector with very low angles of incidence, opening the possibility of using angular discrimination for background reduction.

An active transverse energy filter (aTEF) makes use of the cyclotron radius to achieve angular discrimination by employing a microstructure. Multiple designs of active transverse energy filters are currently being developed within the KATRIN collaboration. This includes the scintillating aTEF (scint-aTEF), which is a 3d printed scintillating microstructure combined with an array of single photon avalanche diodes (SPAD-array).

In this thesis simulations are used to investigate the optimal dimensioning of the scint-aTEF and to give an estimation on the impact that such an aTEF would have on the neutrino mass sensitivity of the KATRIN experiment.

Zusammenfassung

Das **Ka**rlsruhe **Tri**tium **N**eutrino Experiment (KATRIN) dient der direkten Messung der Neutrinomasse mit einer Sensitivität unterhalb eines Elektronvolts. Dazu wird die Energie von β-Elektronen aus dem radioaktiven Zerfall von Tritium durch einen elektrostatischen Filter mittels magnetischer adiabatischer Kollimation (MAC-E-Filter) mit hoher Genauigkeit vermessen.

Aktuell is die Sensitivität des Experiments hauptsächlich durch die statistische Unsicherheit bestimmt, welche von einer höher als erwarteten Untergrundrate stammt. DIe zur Zeit bevorzugte Hypothese für die Entstehung des Untergrunds beinhaltet die Ionisation von Rydberg-Atomen durch die Schwarzkörperstrahlung im Hauptspektrometer. Ein solcher Untergrund würde am Detektor mit sehr kleinen Einfallswinkeln auftreten, was die Möglichkeit eröffnen würde, den Untergrund über seine Winkelverteilung vom Signal zu trennen.

EIn aktiver Transversalenergie-Filter (aTEF) nutzt den Zyklotron-Radius um mit einer Mikrostruktur eine Winkelunterschiedung zu erreichen. Verschiede Versionen eines solchen Filters werden in der KATRIN-Kollaboration entwickelt. Ein Ansatz davon ist der szintillierende aTEF (scint-aTEF). Dieser besteht aus einer 3d-gedruckten szintillierenden Mikrostruktur und einem Raster von Einzelphotonen-Avalanche-Dioden (SPAD-Array).

In dieser Arbeit wird anhand von Simulationen auf die optimale Dimensionierung des scint-aTEFs behandelt und eine Einschätzung der damit erreichbaren Verbesserung der Neutrinomassen-Sensitivität im Rahmen des KATRIN Experiments gegeben.

1. Neutrinos and β-decay

1.1 Neutrinos

Neutrinos are light-weighted electrically neutral particles with spin $\frac{1}{2}\hbar$. Their exact mass has yet to be determined. They only interact through the weak nuclear force and through gravity. Therefore they rarely interact with matter directly, which makes them difficult to detect.

The existence of neutrinos had been postulated by W. Pauli in 1930 [Pau30]. Soon thereafter, E. Fermi incorporated the neutrino into a four point interaction theory to describe β-decay in 1934 [Fer34]. The first experimental confirmation of the neutrino took place in 1956 [CRH$^+$56].

Pauli had made his prediction based on the observed kinematics of nuclear β-decay, which, at that time, were not in accordance with theory. In β-decay, a neutron is converted into a proton, releasing an electron and an electron antineutrino. Without the involvement of an antineutrino, the energy and momentum for both decay products (the proton / nucleus and the electron) would be fully determined by overall conservation of energy and momentum with only the direction of the emitted particle being undetermined. In that case, the kinetic energy of the electron would be close to the total amount of released energy. The much heavier proton / nucleus would absorb the same amount of momentum as the electron, but in contrast require very little kinetic energy to do so. However, the emitted β-electrons were not observed to be monoenergetic but rather follow a continuous spectrum of energies. This made Pauli postulate the existence of a third, neutral particle involved in the process.

Neutrinos have since become part of the standard model of particle physics, which describes the fundamental particles and their interactions in a framework of symmetries under gauge transformations. The particles described in the standard model are "up" and "down" type quarks (three generations) and three generations of leptons (electron, muon, tau and their corresponding neutrinos). All these particle are fermions, meaning they have half-integer spin. In addition to fermions, the standard model also includes gauge bosons, which mediate forces between the fermions. These include the photon γ and the Z and W bosons for the electroweak force and gluons for interactions through the strong force. Furthermore, the standard model includes the Higgs boson, rising from the Higgs field, which is used for spontaneous symmetry breaking of the $\mathrm{SU}_L(2)$ group and the mass acquisition of particles.

The weak nuclear force violates parity by not coupling to the left- and right-handed fermions equally. As a consequence, the left handed fermions enter the standard model as weak isospin doublets: $(\nu_i, i)^T$ for leptons, where i describes the three lepton generations e, μ, τ. The components of these isospin doublets are associated with a weak isospin and transform under the $\mathrm{SU}_L(2)$ group.

The right handed fermions u_R, d_R, e_R, on the other hand, have no weak isospin associated with them and transform as singlets under $\mathrm{SU}_L(2)$. No interaction with right handed

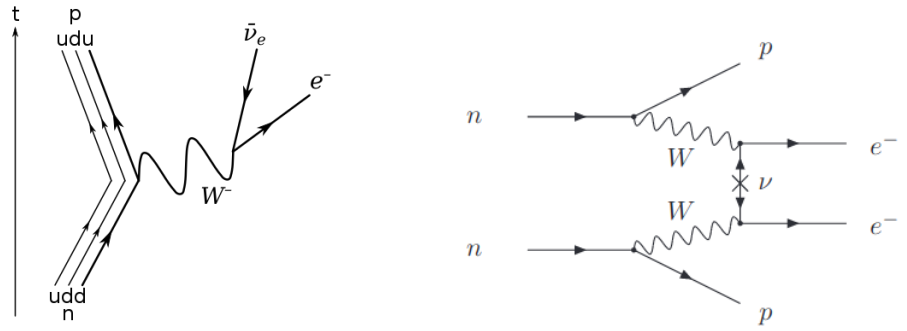

(a) **(b)**

Figure 1.1: (a) The Feynman diagram corresponding to a β^--decay. A down quark from a neutron is turned into an up quark, changing the neutron into a proton. In the process a W boson is emitted, which decays into an electron and an electron antineutrino. Figure from [Hol07]. **(b)** Feynman diagram for a hypothetical neutrinoless double beta decay. In this case the anti neutrinos act as virtual particles which annihilate each other. This is only possible if the neutrino acts as its own antiparticle, violating lepton number conservation. Figure from [Wor+22].

neutrinos has been observed in nature and as a result, these are not part of the standard model.

The $W^\pm$ bosons act on the weak isospin and therefore require an isospin doublet. This means that they only couple to left handed fermions and right handed anti fermions. $W^\pm$ bosons can turn an "up" type quark into a "down" type quark and vice versa. Furthermore, they can turn neutrinos into their corresponding "electron" type lepton and vice versa.

$W^\pm$ boson are the exchange particles in β-decay: A down quark of a neutron is turned into an up quark, which changes the neutron into a proton. In this process a virtual W^- boson is emitted, which decays into an electron and an electron antineutrino. This process is shown in figure 1.1a.

The standard model does not include mass terms of the form $m\bar{\Psi}\Psi = m\bar{\Psi}_R\Psi_L + m\bar{\Psi}_L\Psi_R$ as those terms would violate the $\mathrm{SU}_L(2)$ symmetry due to the different transformation behavior of left- and right handed fermions under this symmetry. Instead, leptons in the standard model acquire their mass by coupling to the Higgs field, which has a non-zero vacuum expectation value. This Yukawa copuling can be written as

$$\begin{pmatrix} \bar{\nu}'_i \\ \bar{e}'_i \end{pmatrix}_L \phi\, \Gamma'_{ij}\, e_{R,j} + \text{h.c.}\,, \tag{1.1}$$

where ϕ is a Higgs doublet, which transforms under $\mathrm{SU}_L(2)$ in such a way that the combined term $(\bar{\nu}'_i, \bar{e}'_i)^T\phi$ is conserved under $\mathrm{SU}_L(2)$ symmetry. The indices i and j describe the three lepton generations e, μ, τ and Γ'_{ij} are complex coupling constants. The "$'$" denotes that eq. (1.1) is given in a flavor basis, which does not necessarily correspond to the mass basis. Because of the $\mathrm{SU}_L(2)$ symmetry, the coupling matrix Γ'_{ij} can be diagonalized using a unitary transformation to align the flavor basis with the mass basis. For the "up" and "down" type quarks, the process for mass acquisition works in a similar way. However, because both "up" and "down" type quarks have mass, they can not be diagonalized at the same time, leading to possible flavor changes in interactions with $W^\pm$ bosons, which are described by the CKM-matrix. As right handed neutrinos are not part of the standard model, there is currently no mass generation for neutrinos implemented in the standard model. Instead, the standard model assumes that they are massless.

Recent observations have shown that neutrinos can switch flavors when traveling over large distances [SFH+98][SAA+01]. These neutrino oscillations can be explained by a

rotation between the flavour and mass basis with regard to each other. Mathematically, this corresponds to a unitary transformation U_{ij}, where i describes the three lepton flavors e, μ, τ and j the three neutrino masses m_1, m_2, m_3. When an electron neutrino is created, from a W boson, it is created in a flavor eigenstate, e.g. ν_e, which is a superposition of the three mass eigenstates $\tilde{\nu}_1, \tilde{\nu}_2, \tilde{\nu}_3$:

$$|\nu_e\rangle = \sum_{j=1}^{3} U_{ej} \, |\tilde{\nu_j}\rangle \ . \tag{1.2}$$

When propagating through space, the states evolve according to the time evolution operator

$$\tilde{U}(t) = e^{-i\hat{H}t/\hbar} . \tag{1.3}$$

In the mass eigenbasis the time evolution can be written as

$$|\Psi(t)\rangle = e^{-i\hat{H}t/\hbar} \, |\Psi(0)\rangle = \sum_{i=1}^{3} e^{-iE_{i,\mathrm{tot}}t/\hbar} \, |\tilde{\nu_i}(0)\rangle \ . \tag{1.4}$$

This means that the complex phase of mass eigenstates with different energies (masses) will evolve at different speeds. Measuring the neutrino flavor after a long time of propagation requires the evolved state to be transformed back into the flavor basis. If there is a non-zero difference between the neutrino masses, the evolved mass eigenstates will have gained different relative phases during their propagation. Back transformation into the flavor basis will then in general no longer yield a pure electron neutrino but rather a superposition of all three neutrino flavors, which explains the observed neutrino oscillations in agreement with experiments.

Neutrino oscillations can not measure the neutrino mass directly but only the differences in neutrino mass squares. Therefore, they can only set a lower limit for the neutrino masses given by the size of the mass differences, while in principle still allowing one of the masses to be zero. The mass differences obtained from neutrino oscillations are currently $\Delta m^2_{21} = (7.53 \pm 0.18) \cdot 10^{-5} \mathrm{eV}^2/c^4$ and $\Delta m^2_{32} = (2.44 \pm 0.03) \cdot 10^{-3} \mathrm{eV}^2/c^4$ [Wor+22].

Cosmological observations place an upper limit of $\sum_{i=1}^{3} m_{\nu_i} < 0.12\,\mathrm{eV}/c^2$ (95 %C.L.) on the neutrino mass. [PYB+15]. A more direct way to measure the neutrino mass is the observation of the energy spectrum from β-decay as it does not rely on cosmological models. Measurements of the β-spectrum using a MAC-E spectrometer have so far yielded an upper limit of $m_{\nu_{e,\mathrm{eff}}} < 0.8\,\mathrm{eV}/c^2$ (90 % C.L.) [ABB+22a]. As an alternative to the MAC-E filter, cyclotron radiation emission spectroscopy can be used for measuring the β-spectrum [EBB+22][EBB+23].

Other experiments look for a neutrinoless double beta decay. In this scenario, two neutrons of a heavy nucleus would simultaneously decay and the two antineutrinos would annihilate each other as virtual particles (see figure 1.1b). In such a case the neutrino must be its own antiparticle, opening the possibility for a Majorana mass term.[BG15]

1.2 β-decay

This section closely follows the description and argumentation of [KBD+19].

The differential β-decay spectrum for molecular tritium can be described using Fermi's golden rule for the transition into a continuum of states:

$$\frac{\mathrm{d}\Gamma}{\mathrm{d}E} = \frac{2\pi}{\hbar} \left| \langle f | \, H' \, | i \rangle \right|^2 \rho(E) \, , \tag{1.5}$$

where E is the kinetic energy of the electron, $|f\rangle$ and $|i\rangle$ are the final and initial states, $\rho(E)$ is the phase space density for a given energy, H' is the part of the Hamilton operator perturbing the free evolution and therefore causing the transition and the total decay rate Γ, which is defined as

$$\Gamma = \left.\frac{\mathrm{d}N}{\mathrm{d}t}\right|_{t=0} . \tag{1.6}$$

To calculate the differential decay rate from the standard model, the squared matrix element $|\langle f| H' |i\rangle|^2$ for the transition from an initial state $|i\rangle$ to a final state $|f\rangle$ must be known as well as the phase space density $\rho_{\mathrm{PSD}}(E)$ of the final states. If there are multiple states with the same observed quantities, the average over all initial states and the sum over all final states must be taken. Unobserved quantities can be, for example, electron spin, momentum direction or the final excitation of the molecule and in general depend on the experimental setup.

For β-decay, the squared matrix element $|\langle f| H' |i\rangle|^2$ can be factorized into two separate parts. These parts represent two processes, which happen mostly independent from each other and are only linked by overall conservation of energy, momentum etc. The first part describes the nucleus, where a neutron decays into a proton, an electron and an electron antineutrino through the weak force. The second part describes the reaction of the suddenly changed daughter molecule, which can lead to different amounts of energy being absorbed by the daughter molecule, which then will not be carried by the electron or the antineutrino.

The nuclear part can be described by a four point interaction using the Fermi coupling constant G_F. Its value is given by $G_{F_0} = G_F/(\hbar^3 c^3) \approx 1.166 \cdot 10^{-5}\,\mathrm{GeV}^{-2}$ [Wor+22]. This is possible because the energy transferred by the $W^{\pm}$ boson is much lower than the mass of the W boson ($m_W \approx 80\,\mathrm{GeV}/c^2$). The nuclear matrix element $\mathcal{M}_{\mathrm{nuc}}$, already including the summation over spin states, can be written as

$$|\mathcal{M}_{\mathrm{nuc}}|^2 = (g_v^2 + 3g_a^2) \cdot |V_{ud}|^2 , \tag{1.7}$$

where $g_v = 1$ and $|g_a| \approx 1.247$[ŠDF08] describe vector and axial couplings and $|V_{ud}| = \cos(\theta_C) \approx 0.97425$ is the coupling constant between the up and down quark, which can also be expressed by the Cabbibo angle θ_C.[KBD+19]

The second part describes the excitation state of the daughter molecule after the β-decay. As the β-decay turns a neutron into a proton, the electric charge of the nucleus is abruptly changed. This can be described as a sudden approximation. In this approximation, the wave function for the electrons (typically in the ground state of the mother atom) stays the same. However, due to the now changed electric charge of the nucleus, the wave function now is a superposition of many energy eigenstates of the daughter molecule. The transition probability for this process can be calculated from the scalar product of the wave function and the new energy eigenstates.

In addition to exciting the electron shell, the recoil of the β-decay can also lead to vibrational and rotational excitations of the resulting $^3\mathrm{HeT}^+$ molecule. Taken together, these effects give rise to a final state distribution (FSD), which describes the transition probability P_i for each final state energy V_i. The β-spectrum can then be viewed as a weighted sum over all these individual spectra, each one with their own effective Endpoint $E_{\mathrm{eff}} = E_0 - V_i$. The endpoint E_0 is the maximal possible kinetic energy the electron can have in the case that the daughter molecule is in its ground state and the neutrino is massless. It differs from the total released energy Q by the recoil energy of the daughter molecule, which near the endpoint is $E_{\mathrm{recoil}} \approx 1.72\,\mathrm{eV}$.[OW08][KBD+19]

The emitted β-electron is not expected to interact much with the electron shell. However, it will still see the electric potential of the daughter nucleus with atomic number $Z = 2$,

although partially shielded by the electron shell. This is described by the Fermi function $F(Z,E)$. Using an approximation for the relativistic version near the endpoint, the Fermi function can be written as [Sim81]

$$F(Z,E) = \frac{2\pi\eta}{1-e^{-2\pi\eta}}(1.002037 - 0.001427\frac{pc}{E+m_e c^2}) \tag{1.8}$$

with

$$\eta = \frac{\alpha Z}{beta}, \tag{1.9}$$

where α is the fine structure constant, Z the atomic number of the daughter nucleus and β is the relativistic velocity v/c.

The kinecic phase space density $\rho(\vec{p})$ in momentum space can be expressed by

$$\mathrm{d}n = \rho(\vec{p})\,\mathrm{d}^3\vec{p} = \frac{\mathrm{d}^3\vec{p}}{(2\pi\hbar)^3} = \frac{4\pi\,p^2\mathrm{d}p}{(2\pi\hbar)^3}\,, \tag{1.10}$$

where n is the number of states in phase space, $\vec{p}$ is the momentum given as a three vector and p is the magnitude of the momentum vector. Using the relativistic relation between momentum p and total energy $E_{\mathrm{tot}} = E_{\mathrm{kin}} + mc^2 = \sqrt{p^2c^2 + m^2c^4}$ for a particle, eq. (1.10) can be written in terms of the total energy:

$$\rho(E) = \frac{4\pi}{(2\pi\hbar c)^3} E_{\mathrm{tot}}\sqrt{E_{\mathrm{tot}}^2 - m^2c^4}\,. \tag{1.11}$$

Integrating over the phase space density of the neutrino[1] under the requirement of energy conservation $\delta^{(1)}(E_0 - E - V_i - E_{\nu,\mathrm{tot}})$ fixes the total neutrino energy $E_{\nu,\mathrm{tot}}$ in terms of the kinetic electron energy E.

Combining the different parts mentioned above, the differential β-spectrum can be described by

$$\begin{aligned}\frac{\mathrm{d}\Gamma}{\mathrm{d}E} = \underbrace{\frac{G_{F_0}^2\,|M_{\mathrm{nuc}}|^2}{2\pi^3\hbar}}_{\substack{\text{constants}\\ \text{and nuclear}\\ \text{process}}} \underbrace{\cdot F(Z,E)}_{\substack{\text{screening}\\ \text{of emitted}\\ \text{electron}}} \cdot \underbrace{(E+m_ec^2)\sqrt{(E+m_ec^2)^2 - m_e^2c^4}}_{\text{phase space of electron}} \\ \cdot \underbrace{\sum_i}_{\substack{\text{sum over}\\ \text{final states}}} P_i \underbrace{(E_0 - E - V_i)\sqrt{(E_0-E-V_i)^2 - m_\nu^2c^4}}_{\text{phase space of antineutrino}} \cdot \underbrace{\Theta(E_0 - E - V_i - m_\nu c^2)}_{\substack{\text{kinetic energy of electron}\\ \text{must be positive}}}\,,\end{aligned} \tag{1.12}$$

where the Θ-function ensures that the kinetic energy of the electron can not become negative. A visualization of this spectrum is shown in figure 1.2.

Because the flavor and mass eigenbasis of the neutrino are rotated against each other[2], the resulting electron antineutrino $\bar{\nu}_e$ will be detected in one of its mass eigenstates m_1, m_2 or m_3. The probability for this is given by $|U_{ej}|^2$, where $j = 1,2,3$ describes the three neutrino masses. The β-spectrum can therefore be considered as the sum of three distinct β-spectra, one for each neutrino mass. From neutrino oscillations, the mass difference

[1] In principle, an integration over the phase space of the daughter nucleus must also be performed. Momentum conservation in all three dimensions fixes the daughter's momentum vector, such that the phase space density is given as $\frac{1}{(2\pi\hbar)^3}$. This factor is canceled when averaging over the initial states of the mother nucleus.

[2] This is indicated by neutrino oscillations, see section 1.1.

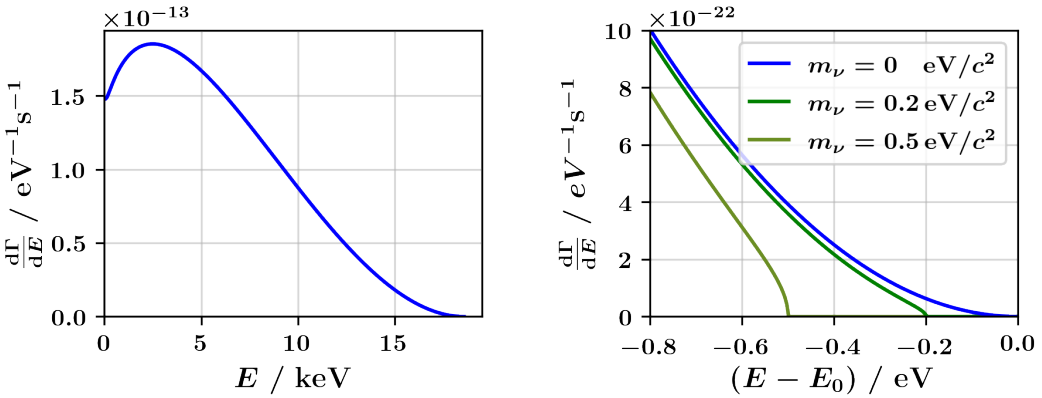

Figure 1.2: Differential β-spectrum for the decay of Tritium. Γ denotes the total decay rate, E is the kinetic energy of the released electron and $E_0 \approx 18.6\,\mathrm{keV}$ describes the endpoint of the spectrum. For illustration purposes, the final state distribution is omitted here. **(a)** Differential spectrum. **(b)** Zoomed in version of (a) showing the distortion in the spectrum caused by a neutrino mass for the cases $m_\nu = 0.5\,\mathrm{eV}$ and $m_\nu = 0.2\,\mathrm{eV}$ compared to the reference case of $m_\nu = 0\,\mathrm{eV}$.

between these mass eigenstates is known, which is much less than the KATRIN experiment can resolve. The incoherent sum

$$m_\nu^2 = \sum_{j=1}^{3} |U_{ej}|^2 m_j^2 \tag{1.13}$$

therefore describes an effective electron neutrino mass, which is measured at the KATRIN experiment.[KBD+19]

Further corrections can be made to the β-spectrum, as described in [KBD+19].

A non-zero neutrino mass causes a distortion in the differential β-spectrum caused by a smaller neutrino phase space. This distortion is most noticeable near the endpoint, where the maximum available energy for the electron is decreased when a higher amount of energy is required to create the antineutrino with a non-zero mass. Notably, also the shape of the spectrum is altered near the endpoint. This is shown in figure 1.2b.

2. The KATRIN Experiment

The **Ka**rlsruhe **Tri**tium **N**eutrino (KATRIN) experiment measures the β-decay spectrum of molecular tritium to a high accuracy to determine the neutrino mass. It is based on previous experiments in Mainz [WDB$^+$99] and Troisk [LAB$^+$99]. The design target for KATRIN is reaching a sensitivity[1] of $\sigma_{m_\nu} = 0.2\,\mathrm{eV}/c^2$ at a 90 % confidence level (C.L.) after three years of data taking, spread out over 5 calendar years [AAB$^+$05]. Data taking has started in April 2019. The first two measurement campaigns have been published, setting an upper bound of $m_\nu < 0.8\,\mathrm{eV}/c^2$ (90 % C.L.) on the neutrino mass [AAA$^+$19][ABB$^+$22a]. In the subsequent time data taking at KATRIN has continued, increasing the statistics on the β-spectrum.

The KATRIN experiment consists of several sections, which are shown in figure 2.1. Electrons emitted from β-decay start in the windowless gaseous tritium source (WGTS) and are guided along magnetic field lines towards the main spectrometer (MS). Along the way the pressure is reduced by many orders of magnitude in the transport and pumping section until the pressure level is at an ultra high vacuum (UHV). In the main spectrometer an electrostatic retarding potential acts as a high pass filter for the β-electrons. Magnetic adiabatic collimation is used in the spectrometer to align the electron momentum with the direction of the field lines (MAC-E-filter). Electrons with energies above the applied retarding potential are counted by the focal plane detector (FPD).

2.1 The Windowless Gaseous Tritium Source (WGTS)

The Windowless Gaseous Tritium Source (WGTS) uses gaseous molecular tritium (T_2) and has a luminosity of $\approx 10^{11}$ decays per second. Tritium is used in the experiment because of its low endpoint of $E_0 \approx 18.6\,\mathrm{keV}$ [AAB$^+$05]. It is injected at the center of the WGTS and continually pumped away at either end, circulating in a closed loop with a throughput of $\approx 40\,\mathrm{g/day}$. The WGTS is cooled to 30 K [PHM$^+$20]. This is done to reduce the Doppler shift caused by the thermal motion of the tritium molecules, which adds an uncertainty on the initial energy of the β-electrons.[ABB$^+$22b]

Superconducting magnets create a homogeneous magnetic field of 2.52 T in the source while the electric potential is held at a constant value. The magnetic field is used to guide the electrons on a cyclotron motion along the magnetic field lines. The windowless design of the source means that it is open towards the spectrometer to make a free path for the electrons. The tritium is prevented from reaching the spectrometer by a series of different pumping sections and chicanes, which reduce the amount of tritium by a factor of 10^{14} [PHM$^+$20].

The other side of the WGTS is closed off by the rear wall. It is used for monitoring of the tritium source and contains an adjustable electron source, which is used for calibration measurements.

[1] This is the combined statistical and systematical uncertainty on the neutrino mass.

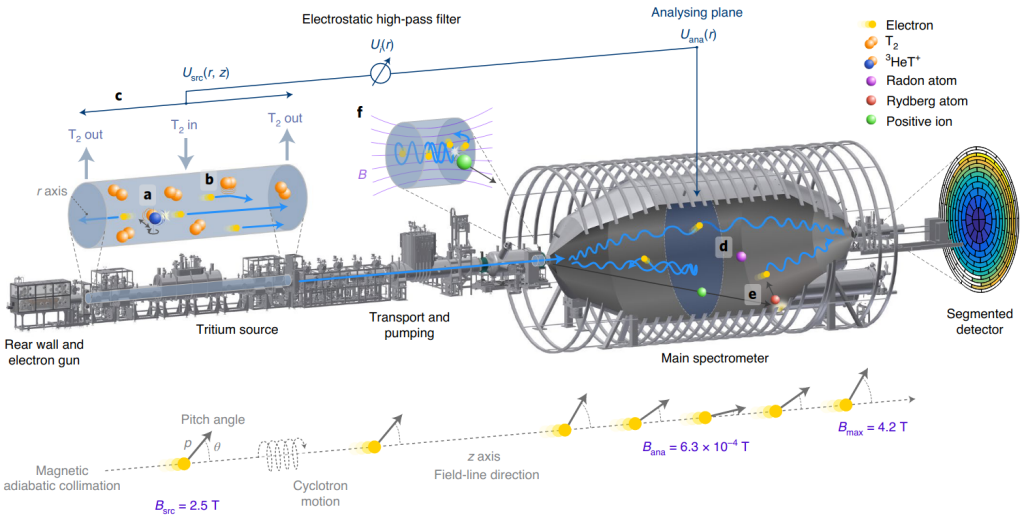

Figure 2.1: Overview of the KATRIN experiment. Electrons stemming from β-decay start in the windowless gaseous tritium source. The β-electrons are then guided along magnetic field lines while performing a helical cyclotron motion around the field lines. Depending on their initial angle they will either be absorbed by the rear wall or transported through the transport and pumping section to the main spectrometer. Electrons emitted with low energies are rejected in the spectrometer by an electrostatic retarding potential. Magnetic adiabatic collimation is used in the main spectrometer to align the electron's momentum with the magnetic field lines. A segmented detector counts the rate of events for a given retarding potential. By varying the retarding potential, an integral β-spectrum can be measured. A strong magnetic field between the main spectrometer and the detector rejects electrons with a large initial pitch angle as those have a large probability of scattering within the source. Figure from [ABB+22a].

2.2 Electron Transport and MAC-E-Filter

The β-electrons are guided by strong magnetic fields, which can reach up to 4.2 T along the beamline. The field lines run all the way from the source to the detector and run in the negative z direction ("upstream"). The electrons follow these field lines while performing a cyclotron motion around them. As electrically charged particles in an electromagnetic field, they will experience the Lorentz force, given by

$$\vec{F}_L = q(\vec{E}_{\text{electric}} + \vec{v} \times \vec{B}) \,, \tag{2.1}$$

where q is the electric charge of the particle, $\vec{E}_{\text{electric}}$ and $\vec{B}$ are the electric and magnetic fields and $\vec{v}$ is the particle's velocity.

In the absence of an electric field this means that the energy of the particle is conserved as the cross product $\vec{v} \times \vec{B}$ always ensures that the force is perpendicular to the motion of the particle. If additionally the magnetic field is homogeneous, the particle's motion can be described by a helical trajectory. Using Newton's second law of motion

$$\vec{F} = \frac{\mathrm{d}\vec{p}}{\mathrm{d}t} \tag{2.2}$$

the properties of this trajectory can be calculated. Using a magnetic field oriented along

the z-direction ($\vec{B} = B_z \vec{e}_z$), this results in

$$R_{\text{cyc}} = \frac{p_\perp}{|qB_z|} \tag{2.3}$$

$$h_{\text{cyc}} = \frac{2\pi p_\parallel}{|qB_z|} \tag{2.4}$$

$$\omega_{\text{cyc}} = \frac{|qB_z|}{\gamma m_e}\,, \tag{2.5}$$

where R_{cyc} is the cyclotron radius, h_{cyc} is the advancement parallel to the field lines during one revolution, ω_{cyc} is the cyclotron frequency and $p_\perp = p\sin(\theta)$ and $p_\parallel = p\cos(\theta)$ are the perpendicular and parallel components of the momentum, which can be expressed through the total momentum p and the pitch angle θ between the particle's motion and the magnetic field lines.

For "slow" changes in the magnetic field, i.e. the relative change in the field is small at the scale of the cyclotron motion, the magnetic flux Φ enclosed by the particle's motion

$$\Phi = \int \vec{B}\,\mathrm{d}\vec{A} = B\pi R_{\text{cyc}}^2 \tag{2.6}$$

is conserved as an adiabatic invariant [Jac99, p. 592f]. Written more concisely, this means that

$$\frac{p_\perp^2}{B} = \text{const.} \tag{2.7}$$

for a particle in a slowly changing magnetic field. Furthermore, it can be shown that eq. (2.7) also holds under longitudinal acceleration.[2]

In the context of the KATRIN experiment, adiabaticity can be assumed[3] and the retarding potential only acts in the longitudinal direction. This means that eq. (2.7) holds individually for each β-electron while it travels through the beamline of the KATRIN experiment.

The adiabatic invariant from eq. (2.7) connects the electric and magnetic field of two places along the beamline with the pitch angle θ in those two places. Written in terms of the angle θ, this yields

$$\sin(\theta_f) = \sqrt{\frac{B_f}{B_i}\frac{E_i(\gamma_i+1)}{E_f(\gamma_f+1)}}\sin(\theta_i)\,, \tag{2.8}$$

where the indices i and f are used to describe the initial and final properties. B is the magnetic field, E describes the kinetic energy of the particle and γ is the relativistic factor.

In the case that the magnetic field lines converge, i.e. B becomes larger, the transverse momentum must increase according to eq. (2.7). However, as energy must be conserved, the maximum transverse momentum is limited by $p_\perp \leq p$. This means that particles can be reflected in a converging magnetic field if their initial pitch angle θ is large enough.[4] The point of reflection is then given by an earlier location along the beamline, where angle reaches $\theta = 90°$ for this specific particle.

In the KATRIN experiment, the largest magnetic field is reached at the pinch magnet, which is located between the main spectrometer and the focal plane detector. This magnet

[2] This can be seen from eq. (2.2), which leaves $p_\perp$ unchanged under longitudinal acceleration. One can also explicitly calculate $p'_\perp = \gamma'\beta' mc\sin(\theta')$ where the "′" denotes the quantities after the acceleration and find that γ, β and θ transform in a way such that $p'_\perp = p_\perp$.

[3] Detailed tracking simulations show little difference.

[4] This can be pictured similar to how a strip of paper wrapped around a conical section will change its direction. In this case, the conical section represents the magnetic flux enclosed by the particle's trajectory.

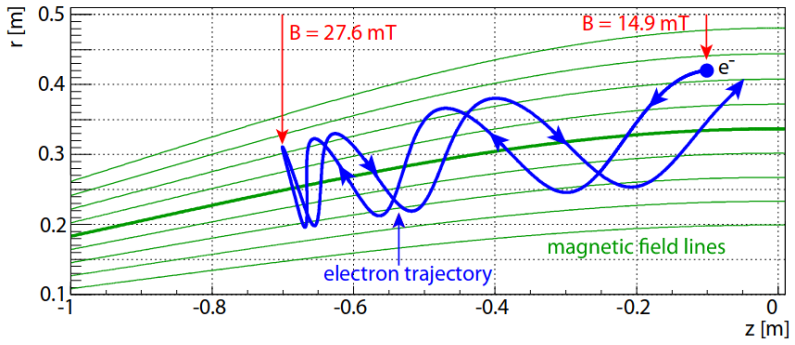

Figure 2.2: Example for magnetic reflection in a converging magnetic field. The field lines shown here are from the pre-spectrometer, which was initially used to filter out the lower energies of the β-spectrum. Figure from [Frä10].

is used to reject β-electrons with large angles as those have a high probability to scatter inelastically with the tritium molecules in the source, resulting in energy loss and an increased energy uncertainty. The maximal initial angle, which is still being transmitted by the pinch magnet, can be calculated to

$$\theta_{\text{max}} = \arcsin\left(\sqrt{\frac{B_{\text{src}}}{B_{\text{max}}}}\right) \approx \arcsin\left(\sqrt{\frac{2.5\,\text{T}}{4.2\,\text{T}}}\right) \approx 51°. \tag{2.9}$$

The change in pitch angle in an adiabatically changing magnetic field is a property that can be used to enhance the energy resolution of an electrostatic filter. For this, two new variables are introduced as defined in[KBD+19]

$$E_{\perp} = E\sin^2(\theta) \tag{2.10}$$

$$E_{\parallel} = E\cos^2(\theta)\,, \tag{2.11}$$

which describe the kinetic energy being split up into a longitudinal and a transverse component described by the angle θ between $\vec{p}$ and $\vec{B}$. When a retarding potential is applied with $\vec{E} \parallel \vec{B}$, the longitudinal momentum of the particle is reduced until it is either reflected ($\theta = 90° \Leftrightarrow p_{\parallel} = 0$) or the particle reaches the maximum retarding potential with $\theta < 90°$. Using eq. (2.8) for the critical angle of 90° at the maximum retarding potential, the transmission condition can be calculated to be

$$\sqrt{\frac{B_{\text{ana}}}{B_{\text{src}}}\frac{E_{\text{src}}\sin^2(\theta_{\text{src}})}{E_{\text{ana}}}\frac{(\gamma_{\text{src}}+1)}{(\gamma_{\text{ana}}+1)}} \leq 1\,, \tag{2.12}$$

where the subscripts $_{\text{src}}$ and $_{\text{ana}}$ are used to describe the magnetic field B, kinetic energy E, relativistic factor γ and pitch angle θ at the source exit and at the analyzing plane (location of maximum retarding potential) respectively. In the non-relativistic case ($\gamma_{\text{src}} \approx \gamma_{\text{ana}} \approx 1$) the transmission condition can be simplified to

$$E_{\text{ana}} \geq \frac{B_{\text{ana}}}{B_{\text{src}}} E_{\perp,\text{src}}\,. \tag{2.13}$$

For $B_{\text{ana}} = B_{\text{src}}$, this means that the minimum kinetic energy E_{ana} required for transmission at the analyzing plane (AP) is given by the initial transverse energy $E_{\perp,\text{src}}$. This way, the retarding potential only measures the longitudinal energy of the particle and not the total amount of energy. In an electrostatic filter using magnetic adiabatic collimation (MAC-E-filter), the magnetic field is reduced at the analyzing plane $B_{\text{ana}} \ll B_{\text{src}}$ to align

Table 2.1: Typical magnetic field settings for selected points along the beamline of KATRIN.

symbol	B/T (typical)	location
B_{src}	2.52	source (WGTS)
B_{ana}	$6.3 \cdot 10^{-4}$	analyzing plane (AP)
B_{pinch}	4.2	pinch magnet
B_{det}	2.4	detector (FPD)

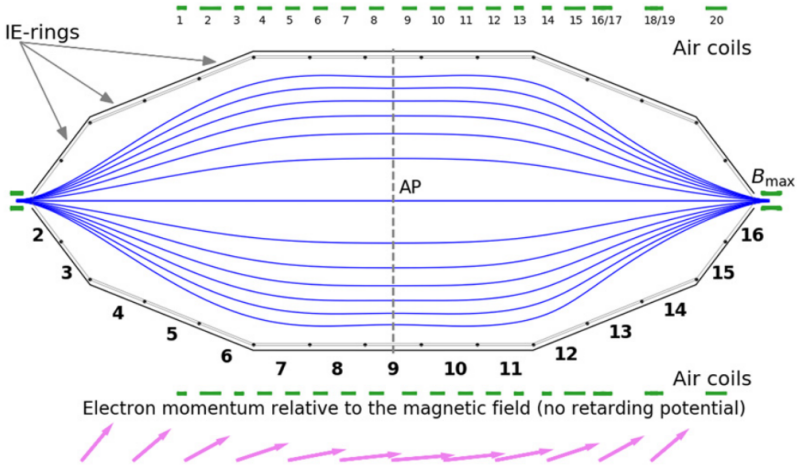

Figure 2.3: Working principle of a MAC-E-filter (electrostatic filter with magnetic adiabatic collimation). β-electrons from the WGTS arrive on the left side of the spectrometer. The analyzing plane (AP), where the retarding potential reaches its maximum, is located in the center of the main spectrometer. Before reaching the analyzing plane, the magnetic field is lowered by several orders of magnitude. This necessitates a spacial increase of the flux tube, hence the large diameter of the spectrometer. During this decrease in magnetic field strength the electron's momentum is aligned with the magnetic field lines through magnetic adiabatic collimation as indicated by the purple arrows. Figure from [ABB+22b].

the particle's momentum with the field lines. This way, the influence of the transverse energy is reduced by a factor of $B_{\mathrm{ana}}/B_{\mathrm{src}}$.

The filter width of the MAC-E-filter describes the difference in effective retarding potential compared to the nominal retarding potential U_{ret} which the particles experience due to their transverse momentum. For a normal (symmetric) analyzing plane in a 6.3 Gauss setting this amounts to

$$\Delta E \approx \frac{B_{\mathrm{ana}}}{B_{\mathrm{src}}} E_0 \sin^2(\theta_{\mathrm{max}}) \approx 2.8\,\mathrm{eV}\,, \tag{2.14}$$

where $E_0 \approx 18.6\,\mathrm{keV}$ describes the endpoint of the β-spectrum and therefore the maximum energy among the electrons. Electrons with a surplus energy $E_{\mathrm{src}} - qU_{\mathrm{ret}}$ greater than the filter width ΔE will always be transmitted while electrons with a surplus energy of $0 < E_{\mathrm{src}} - qU < \Delta E$ will only be transmitted if their angle θ is low enough to fulfill the transmission condition of eq. (2.12).

The low magnetic field around the analyzing plane is shaped by a set of air coils distributed around the main spectrometer. Due to the low required fields, additional air coils have been installed to compensate for the earth's magnetic field.

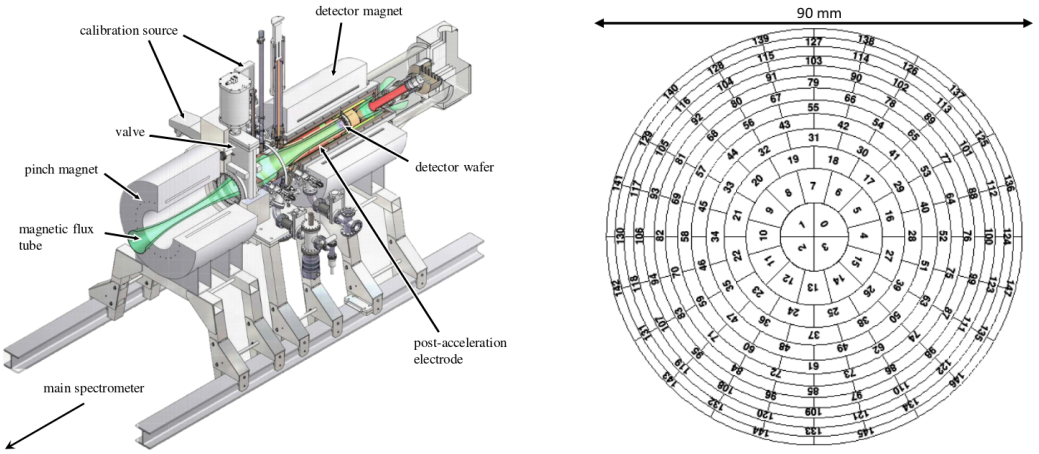

(a) **(b)**

Figure 2.4: The Focal Plane Detector (FPD) is located at the end of the beamline and counts the incoming electrons. **(a)** Schematic of the FPD assembly. The flux tube (shown in green) is the volume in which the β-electrons travel from the source to the detector. A small flux tube corresponds to a large magnetic field. The strongest magnetic field is achieved at the pinch magnet, which reflects electrons with an initial pitch angle larger than 51°. The detector magnet focuses the beam again to keep its size within the beam tube and the diameter of the focal plane detector. A post-acceleration electrode (PAE) increases the electron energy by 10 keV for better detection. Figure from [Hac17]. **(b)** Pixel arrangement of the FPD in concentric rings. Each pixel has an area of 44 mm^2 [ABB+15]. Figure from [Sch20].

2.3 Focal Plane Detector (FPD)

The focal plane detector (FPD) is located at the end of the beamline and counts the arriving electrons. It operates as a PIN-diode and has a diameter of 90 mm [ABB+15]. The detector is segmented into 148 pixels of equal size, which are arranged in a concentric pattern. Each pixel of the detector corresponds to a segment of the flux tube volume along the beamline which is mapped onto the FPD. The spacial resolution is used in the neutrino mass fit to account for radial dependencies such as an increasing background rate towards the outer rings or inhomogeneities in the analyzing plane field.

A post-acceleration electrode (PAE) increases the electon's energy by another 10 keV before the electrons hit the detector with a total energy of ≈ 28.6 keV. This additional energy allows for better distinction between intrinsic detector noise and incoming electrons. As the energy resolution of the detector is larger than 1 keV [ABB+15], the detector itself can not be used to directly measure the differential β-decay spectrum. Instead, the integral β-spectrum is obtained by measuring the rate of β-electrons at different retarding potential settings of the main spectrometer.

3. Background in the KATRIN Experiment

Only a tiny fraction of 10^{-13} of the decays happen in the last 1 eV of the β-spectrum. Even with a source activity of 10^{11} decays per second, this amounts to a rate of only a few millicounts per second (mcps) in the last eV. Therefore, it is essential to keep the background level to a minimum. Currently, the background level exceeds the design value of 10 mcps by more than an order of magnitude.[ABB+22b]

This chapter gives a brief overview of the different background components and their mitigation methods. While many background contributions have been identified and mitigated, background investigations are still ongoing. For more information on the development of the background model see, among others, [Tro19], [Dyb19], [Sch20] and [Hin22]. Figure 3.1 shows a graphical overview for many of the background processes in KATRIN.

3.1 Intrinsic Detector Background

Part of the experiment's background is created in the detector itself, either through the decay of ^{40}K or by muons created in the upper atmosphere by cosmic radiation. A shielding of Pb and Cu protects the detector from interfering β-electrons from the decay of radioactive isotopes. Furthermore, a post acceleration electrode (PAE) is used to accelerate the electrons coming from the main spectrometer (MS) by an additional 10 keV. This shifts the region of interest (ROI) to higher energies, which makes it easier to distinguish β-electrons from intrinsic detector background based on their larger energy deposition in the detector. In addition, the FPD is surrounded by scintillators, which can detect muons and send a

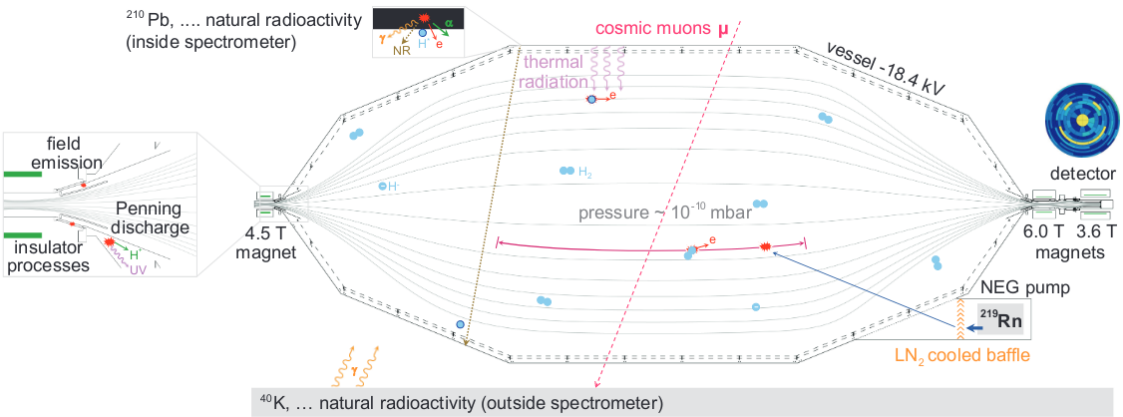

Figure 3.1: Background sources in the KATRIN experiment. Electrons generated on the detector side of the analyzing plane can be accelerated towards the detector. See text for more information on the respective background processes. Figure from [Fra17].

veto signal. In total, the intrinsic detector background could be reduced to $\approx 12\,\mathrm{mcps}$ [LBD+22] if additionally a narrow region of interest is used.[Sch20]

3.2 Radon Induced Background

Radon, stemming from the non-evaporable getter pumps (NEG) on the detector side of the main spectrometer, is another source for background in the KATRIN experiment. The isotopes contributing most to the background are ^{219}Rn and ^{220}Rn due to their short half lives of $T_{1/2}(^{219}\mathrm{Rn}) \approx 3.96\,\mathrm{s}$ and $T_{1/2}(^{220}\mathrm{Rn}) \approx 55.6\,\mathrm{s}$. As part of a primordial nuclear decay chain, they are created through the decay of ^{235}U and ^{232}Th respectively. Because Radon is a noble gas, it does not bond well to the surface of the getter pumps and can escape into the main spectrometer. As neutral particles, the radon isotopes can enter the whole spectrometer volume and thus decay within the flux tube, releasing electrons in the process. Radioactive isotopes with a half life significantly longer than the pumping time of the main spectrometer will mostly be removed from the spectrometer before they can decay.[Har15]

When ^{219}Rn or ^{220}Rn decay into an excited Polonium state via α decay, they can release up to 20 electrons in the process of reaching a new stable configuration [Har15]. With typical energies of 10 eV to 10 keV, these electrons are well above the energy resolution $\Delta E \approx 2.8\,\mathrm{eV}$ of the main spectrometer. With increasing energy only a fraction of those are emitted in a narrow angle with respect to the magnetic field lines to meet the transmission condition for the pinch magnet ($E_{\perp,\mathrm{ana}} < \Delta E$). Electrons with a larger transverse energy are reflected by the pinch magnet and can become trapped in the main spectrometer, oscillating back and forth between the strong magnets at the entrance and exit of the spectrometer. Such a trajectory is shown in figure 3.2.[1]

Electrons can only escape this trap if they either scatter in such a way that their transverse momentum becomes small or if they lose their energy through synchrotron radiation and inelastic scattering until they meet the transmission condition. This process can take several hours. Therefore, these electrons themselves do not lead to an increased background rate but rather secondary and tertiary electrons generated from trapped electrons scattering with residual gas molecules in the main spectrometer could add to the background. The overall contribution of trapped electrons to the background rate has been studied by the use of a short pulsed transverse electric field to remove the stored electrons from the spectrometer. However, this did not significantly reduce the background rate. Therefore the stored electrons are not the main source of background in the KATRIN experiment.[Har15]

To mitigate the background caused by the decay of Radon, baffles cooled by liquid nitrogen have been installed, which block the direct line of sight from the getter pumps to the main spectrometer volume. Emitted Radon will stick to the cooled baffle surfaces for a short amount of time, but long enough to prevent it from decaying in the flux tube volume inside the main spectrometer.[Har15]

3.3 Background Emanating from the Spectrometer Walls

Naturally occurring radioactivity, such as the γ rays from ^{40}K as well as well as high energetic atmospheric muons (created by cosmic rays) can knock out electrons from the spectrometer walls [Fra17]. Shielding against these kind of electrons is achieved by the inner electrode system, which repels electrons back towards the spectrometer walls (figure 3.3). Furthermore, the magnetic field curves the trajectory of those electrons back to the spectrometer wall, such that they do not enter the magnetic flux tube.

[1] In principle, electrons with low energies but large angles can also be trapped between the electric potential of the analyzing plane (AP) and either one of the "pinch" magnets.

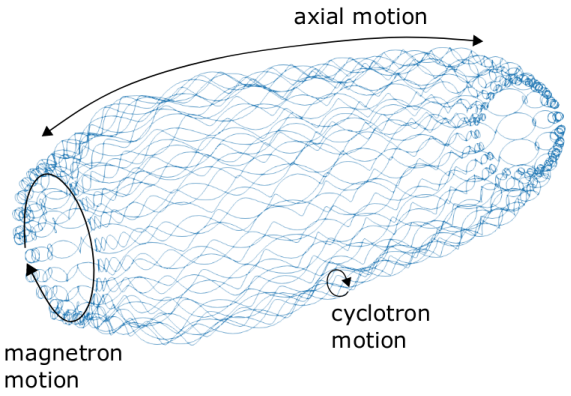

Figure 3.2: Trajectory of a stored electron in the main spectrometer. It is reflected at either end of the spectrometer by converging magnetic field lines. Figure from [Sch20].

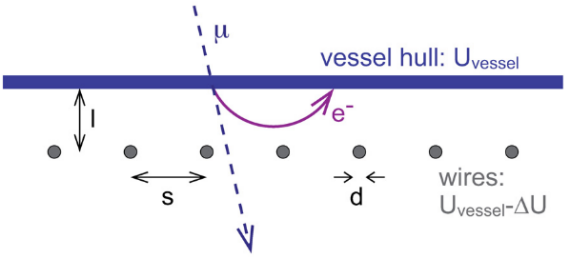

Figure 3.3: Inner electrode system to reject secondary electrons emanating from the spectrometer walls. The two layers (only one is shown) of thin wires are placed on a more negative potential compared to the spectrometer walls. Figure from [Val09].

3.4 Rydberg Mediated Background

To explain the remaining background in the KATRIN experiment, a model using Rydberg atoms stemming from the spectrometer walls was developed [Tro19]. As neutral particles, these Rydberg atoms can propagate through the spectrometer and enter the flux tube. The atoms with electrons in a highly excited state could then be ionized by black body radiation (BBR) emanating from the spectrometer walls. If this ionization takes place downstream of the analyzing plane, the ionized electrons will be accelerated towards the detector by the retarding potential, leading to comparable energies to those of β-electrons. Measurements involving the background dependence on electric and magnetic field settings, pressure and radial distribution indicate that Rydberg atoms could be a source for part of the remaining background.[Hin22]

Rydberg Atoms can be created at the spectrometer walls through the decay of ^{210}Po. In the construction phase of KATRIN, naturally occurring ^{222}Rn could have entered the main spectrometer and implanted ^{210}Pb into the stainless steel when decaying near the spectrometer walls. The decay of ^{210}Po, a successor to ^{210}Pb in the decay chain, emits an α particle when decaying, which can lead to sputtering of surface atoms, such as hydrogen, into the main spectrometer. Some of the sputtered atoms can be in an excited state, leading to neutral Rydberg atoms propagating through the flux tube volume, where they can be ionized by black body radiation (see figure 3.4).[Hin22]

The Rydberg background is in part already reduced by the inner electrode system (see figure 3.3), which creates a strong electric field near the spectrometer walls. This electric field can lead to the ionization of Rydberg atoms near the spectrometer walls, such that the electrons can not enter the flux tube volume (see section 3.3).[Tro19]

The background rate can be further reduced by baking out the spectrometer. This was

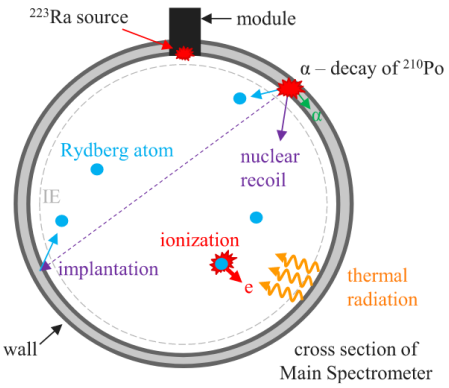

Figure 3.4: Cross section through the main spectrometer showing the mechanism for Rydberg mediated background processes. The recoil α-decay of ^{210}Po sputters atoms into the spectrometer volume, including highly excited hydrogen atoms (Rydberg atoms). These neutral atoms are not affected by the magnetic field and can enter the flux tube located in the middle of the spectrometer (not shown). Black body radiation stemming from the spectrometer walls can ionize the Rydberg atoms, leading to a background of Rydberg electrons measured at the FPD. An additional source of radiation for background investigations is also shown. Figure from [FSB+22].

done between the first and second neutrino mass campaign, which lead to a background reduction of 25 % [ABB+22a]. In the process of baking out, adsorbed gasses and water are removed from the spectrometer walls, which reduced the effect of sputtering from the decay of ^{210}Po.

Another approach to reduce the background rate is to lower the flux tube volume downstream of the analyzing plane. This can be done by the use of a shifted analyzing plane (SAP) [LBD+22], which was introduced in the third neutrino mass campaign (KNM3). In this configuration, the magnetic and electric fields are adjusted to obtain a spacially curved analyzing plane close to the detector side of the spectrometer (figure 3.5). This reduces the flux tube volume on the detector side of the analyzing plane, which leads to a lower background rate. The SAP configuration introduces a radially symmetric but inhomogeneous electric and magnetic field and could potentially lead to non-adiabatic behavior. The radial inhomogeneities can in part be absorbed by a pixel/ring based analysis, such that the inhomogeneities only matter over the scale of the flux tube corresponding to a single detector pixel. Using a shifted analyzing plane, the background at KATRIN could be reduced by a factor of two [LBD+22].

The Rydberg hypothesis would lead to electrons with a low mean initial energy of 15 meV [Sch20], which is much smaller than the energy resolution of the main spectrometer of $\Delta E \approx 2.8\,\text{eV}$ at $B_{\text{ana}} = 6.3\,\text{Gauss}$. Therefore, these Rydberg electrons would arrive at the detector with pitch angles of only a few degrees due to their low transverse momentum.

3.5 Oxygen Autoionization Background Hypothesis

Measurements performed in [Dyb19], [Sch20] and [Hin22] indicate that larger transverse energies must be present in the background than can be explained with the Rydberg hypothesis alone. Therefore, modifications to the Rydberg model have been proposed. One such modification involves auto ionization states of sputtered oxygen atoms. In oxygen, it is possible to reach a semi-stable state, where two electrons are in a highly excited state (planetary atoms). The de-excitation of such a state will lead to ionization of the molecule, releasing an electron with an initial energy of up to a few eV. Two of the initial energies associated with oxygen autoionization are at 425 meV and 495 meV with additional states

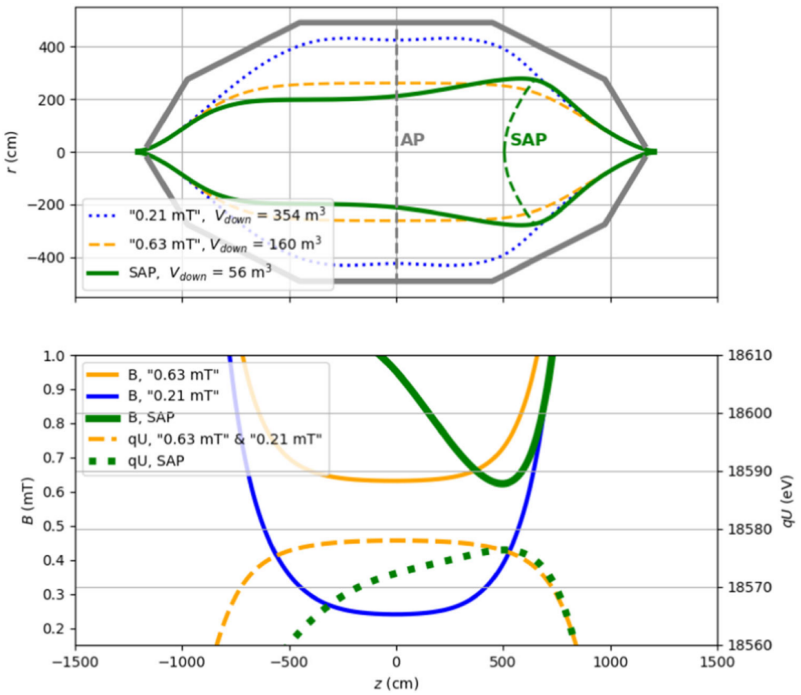

Figure 3.5: Shifted analyzing plane with adjusted electric and magnetic fields to reduce the flux tube volume downstream of the analyzing plane (AP) compared to the symmetric case. Figure from [LBD+22].

above these energies [FEE05]. Under certain conditions, the decay of double Rydberg states could be slow enough that the neutral atoms could reach the center of the spectrometer before decay happens.[Hin22]

While the lower energy levels of oxygen auto ionization introduce larger initial energies for background electrons, this model is neither complete nor final at the moment. Earlier measurements [Dyb19], [Sch20], [Hin22] either indicate or do not exclude larger initial energies being present in the background of KATRIN. This is in agreement with current background investigations by D. Hinz and J. Lauer, which also point to a large non-Rydberg fraction or initial energies larger than 500 meV being present in the background spectrum.

4. Transverse Energy Filters

A Transverse energy filters (TEF) make use of the helical cyclotron motion of charged particles in a homogeneous magnetic field to discriminate particles based on their pitch angle θ. These filters can be employed for electrons with low energies in the $\mathcal{O}$(keV) range, where the angle of the incoming electrons can not be retrieved by other methods such as the use of Cherenkov light or by reconstructing a particle track through multiple layers of the detector.

The cyclotron radius R_{cyc} and height h_{cyc} are described by eq. (2.3) and (2.4) and depend on the pitch angle θ between the particle's trajectory and the magnetic field lines. When employing a plate-like microstructure with channels roughly matching the size of the cyclotron radius and a height less than the cyclotron height, the transmission probability of such a structure will strongly depend on the individual particle's cyclotron radius and height. For an approximately monoenergetic beam, these two properties are directly linked to each other via the angle θ, such that the TEF acts as an angular selective device via the angular dependent transmission probability. In the more general case, two parameters are necessary to describe the transmission probability, e.g. the total kinetic energy E and the angle θ of the electron.

Angular selection is achieved by a fine, grid-like structure, which can make use of both the cyclotron radius $R_{\text{cyc}} \sim \sin(\theta)$ and the cyclotron height $h_{\text{cyc}} \sim \cos(\theta)$ of the electrons. This concept is visualized in figure 4.1. For angles much lower than 90°, angular selection is primarily achieved through the change in cyclotron radius.

The microstructure of the transverse energy filter is placed directly inside the beam. It therefore acts equally across the whole beam and can be employed for angular selection in cases where the individual particles do not oscillate around a common reference trajectory.[1] In the KATRIN experiment, the particles oscillate along the longitudinal guiding magnetic field lines with a beam size much larger than an individual particle's oscillation amplitude (its cyclotron radius). Assuming background electrons created with low energies in the main spectrometer of the KATRIN experiment, they would have an angular distribution shifted towards low angles, caused by the longitudinal acceleration from the retarding potential (figure 4.2). This difference in angular distribution between signal and background electrons opens up the potential of using transverse energy filters in the KATRIN experiment for both background investigation and mitigation.

4.1 Passive Transverse Energy Filters (pTEF)

In a passive transverse energy filter (pTEF), the microstructure (see figure 4.1) is used to filter out particles with large angles, while transmitting most particles with low angles.

[1] This is in contrast to typical applications in accelerator physics, where particles will usually oscillate around a single reference trajectory (assuming a point along the beamline with low energy dispersion), which would enable the use of beam collimation.

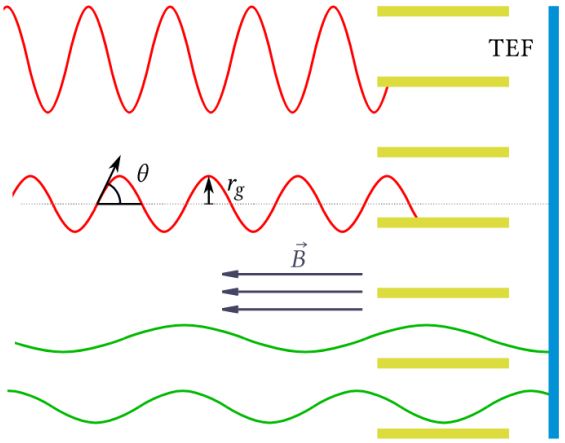

Figure 4.1: Principle of a transverse energy filter (TEF). Monoenergetic particles in a homogeneous magnetic field follow trajectories with different cyclotron radii and heights depending on their pitch angle θ. Electrons with small pitch angles (shown in green) can pass the filter while electrons with large angles (shown in red) are absorbed by the channel walls due to their large cyclotron motion. This results in an angular dependent transmission probability for the transverse energy filter. Figure from [Lau22].

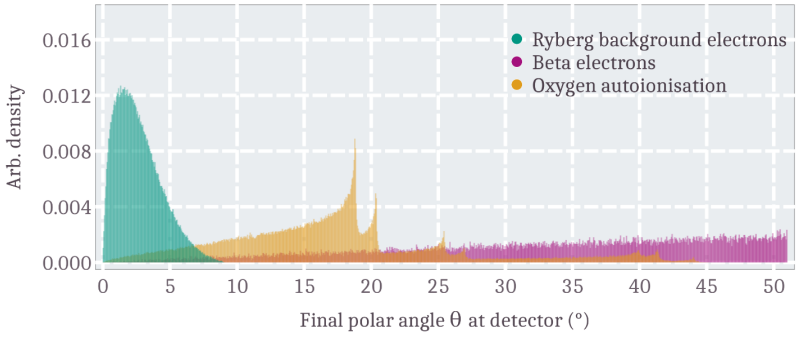

Figure 4.2: Simulated angular distribution at the detector for Rydberg and oxygen autoionization electrons created in the main spectrometer for a magnetic field strength of $B_{\text{ana}} = 5\,\text{Gauss}$ and shown for $B_{\text{det}} = 2.5\,\text{T}$. The angular distribution is shifted towards small angles by the longitudinal acceleration caused by the retarding potential in the main spectrometer. The first two peaks of the oxygen autoionization spectrum correspond to initial energies of the background electrons of 425 meV and 495 meV [FEE05]. An isotropic spectrum $\propto \sin(\theta)$ is shown for the signal electrons as those are created in a comparable magnetic field and therefore do not undergo angular changes. The maximum angle of the β-electrons is determined by the pinch magnet. Figure from [Hin22].

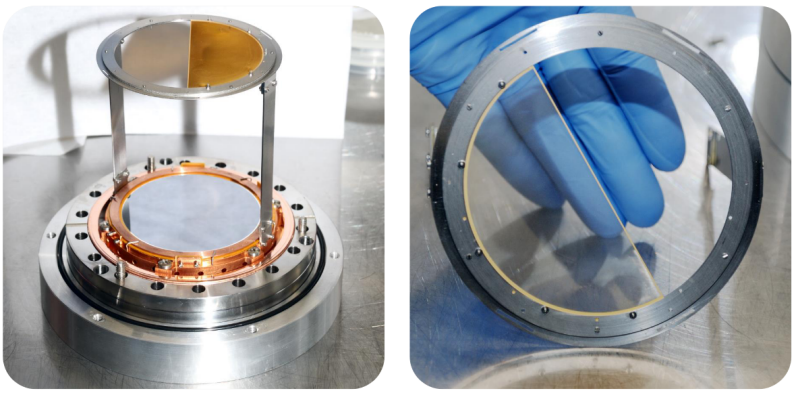

Figure 4.3: The passive transverse energy filter (pTEF) used for background investigations in [Hin22]. The microstructure is made from gold and consists of hexagonal channels with a side length of 100 µm, a height of 250 µm and a wall width of 8 µm. The left view shows the pTEF installed in front of the focal plane detector (FPD). When viewing from the side (left picture) the pTEF (covering the right half of the disc) obstructs the view. When viewed from the front, the pTEF appears mostly transparent (right picture). Figure from [Hin22].

An example for such a microstructure made from gold is shown in figure 4.3. It was used during a pTEF campaign to study the angular distribution of background electrons in KATRIN near the focal plane detector and thereby study the TEF-principle[Hin22]. As described above, the angular distribution at the detector depends on the initial energy of the background electrons at creation in the main spectrometer, the retarding potential and the magnetic field at the analyzing plane (AP). By varying the magnetic field and the retarding potential, different parts of the angular spectrum can be probed with a single pTEF geometry.

In the analysis of the pTEF campaign one makes use of both the reduced transmission characteristics and the angular spectrum of the transmitted electrons. The latter will imprint itself on the measured energy deposition in the focal plane detector (FPD), which is angular dependent due to a dead layer in the detector. Both effects can be used to gain insight into the angular distribution of the background electrons, but requires a detailed analysis including effects such as electron backscattering at the golden pTEF surface. The data from the first pTEF campaign is currently being reanalyzed in greater detail by D. Hinz and J. Lauer and a second pTEF campaign is planned for Winter 2023/24, which would involve a pTEF with two different channel sizes.

4.2 Active Transverse Energy Filters (aTEF)

An active transverse energy filter (aTEF) uses the microstructure itself as a detector. Therefore, particles with large angles have a higher detection probability than particles with lower angles.

Several approaches exist on how such an aTEF could be realized. The original design includes the use of a microchannel plate (MCP) with an accelerating voltage applied between the MCP and the detector. The electrons would, upon hitting the inner channel walls, knock out further electrons, which would be accelerated towards the detector. This cascade of secondary electrons could be detected and its signal distinguished from a single background electron hitting the focal plane detector.[GSD$^+$22]

The silicon aTEF (Si-aTEF) is another approach mentioned in [GSD$^+$22], which is being developed by a group from the Universität Münster. It involves etching hexagonal microchannels directly into a silicon waver, such that the walls function as PIN-diodes,

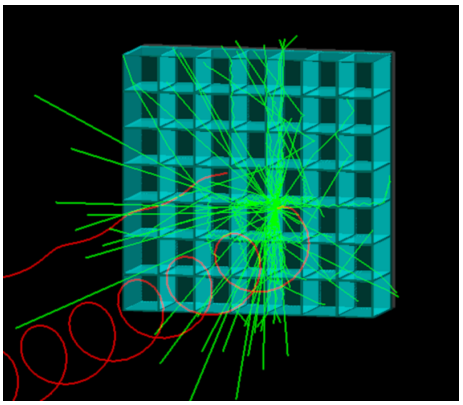

Figure 4.4: Simulation of the scintillating active transverse energy filter (scint-aTEF) in Geant4 [AAA+03; AAA+06; AAA+16]. A subgrid of 7×7 cells is illustrated. The scintillator is shown in a light blue color while a darker color is used for the non-scintillating plastic. A passive layer covers the top of the scintillating grid. The aTEF principle is illustrated by two electron tracks (shown in red) with different pitch angles. The created scintillation photons are shown in green. An array of single photon avalanche diodes (SPAD-array) is placed behind the grid-like structure for detection of the scintillating photons.

Table 4.1: Default parameters for the scint-aTEF.

symbol	default value	description
a_{cell}	variable	cell width
h_{scint}	300 µm	height of scintillator grid
h_{top}	10 µm	height of passive top layer [a)]
$h_{\text{backplate}}$	10 µm	height of passive backplate
d	10 µm	wall width

[a)] can be removed to increase signal efficiency

similar to how the focal plane detector (FPD) of the KATRIN experiment operates. This would require a passive layer covering the bottom of the channels to prevent transmitted electrons, i.e. electrons which did not hit a channel wall, from being detected.

Another approach involves the use of a scintillator for the active microstructure. This scintillating aTEF (scint-aTEF) is being developed at the Karlsruhe Institute of Technology (KIT) and is described in more detail in the following section.

4.3 The Scintillating Active Transverse Energy Filter (scint-aTEF)

The scintillating active transverse energy filter (scint-aTEF) uses a 3d printed plastic scintillator as an active microstructure for angular discrimination. Its main components are a scintillating grid and an array of single photon avalanche diodes (SPAD-array) to detect the scintillation light. A thin layer of transparent non-scintillating plastic is placed between the scintillator grid and the SPAD-array to shield it from transmitted electrons with low pitch angles.

When an electron is absorbed by the scintillating grid, the scintillator converts some of the deposited energy into light. These photons are then guided by the scintillating structure to the SPAD cells, where they can be detected as a localized cluster of photons. The design of the scint-aTEF is visualized in figure 4.4.

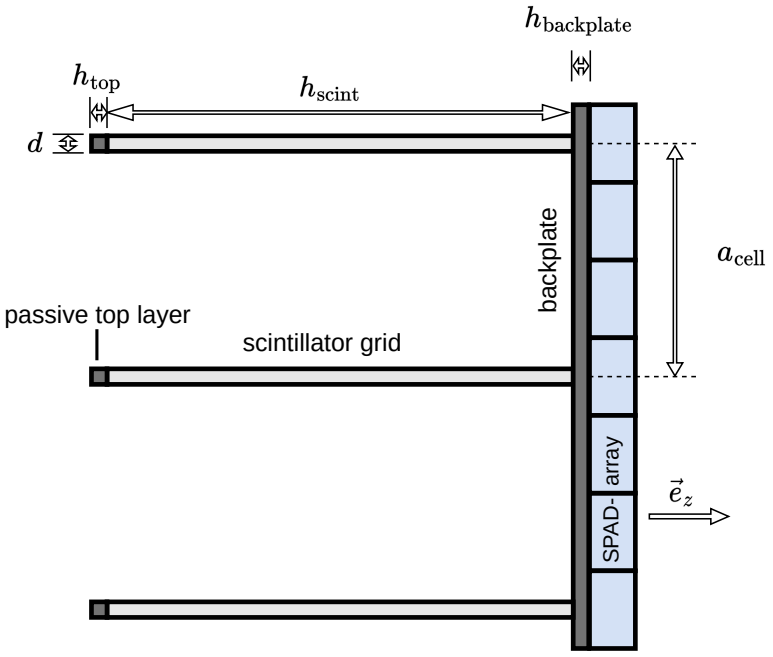

Figure 4.5: Side view of the geometry for the scint-aTEF.

4.3.1 The Scintillator Grid

The scintillating microstructure is a square grid with a height of $h_{\text{scint}} = 300\,\mu\text{m}$, a wall width of $d = 10\,\mu\text{m}$ and a cell width of $a_{\text{cell}} \approx 100$ to $150\,\mu\text{m}$ (figure 4.5). The height of the grid is chosen based on observations made in section 6.2. It can be lowered if necessary. In such a case, the width of the scint-aTEF cells have to be adjusted. The wall width should be as low as possible to ensure good angular discrimination while at the same time it must both provide enough structural stability and be able to completely absorb 18.6 keV electrons. The cell width is taken to be a "variable" parameter, which can be optimized for maximum effectiveness of the scint-aTEF under different initial conditions. 3d printing using two-photon absorption will be used to create this microstructure grid.

Two-photon absorption printing uses light of twice the wavelength (half the energy) necessary for polymerization of the viscous printing material (resin). If the printing material is transparent to the supplied wavelength, polymerization can only occur when two photons are absorbed at the same time. This requires a high flux of photons, which can be created by focusing a high intensity laser beam onto a small spot in 3d space. The intensity of the laser beam can be adjusted in such a way that polymerization can only occur in the direct vicinity of the focal point. This enables 3d printing at the sub-micrometer scale [MTW14]. [MNK97]

3d printable plastic scintillator resin consists of several components. The main ingredient of the resin consists of a monomer. A photoinitiator is used to start the polymerization process, turning the monomers into a solid polymer when exposed to the correct wavelength. For the scintillation process, molecules with aromatic compounds are used, as those structures generate the necessary optical properties for the molecules [KKL$^+$22]. Finally, wavelength shifting molecules are used to move the wavelength of the scintillation photons to lower energies, where the scintillator becomes transparent for the scintillation light.[MHH$^+$93], [SKL$^+$18]

Using a scintillator as the basis for the aTEF has the benefit of using a material with a low atomic number, which reduces the backscattering probability for electrons [Gei22]. At the

same time, finding a resin composition both suitable for two-photon absorption printing and with a high light yield poses a challenge and is an ongoing process. Currently, different resin compositions and printing parameters are being tested for their achievable light yield by A. Huber.

Another challenge is the outgassing rate of the plastic scintillators. Early investigations have shown that the initial outgassing rate lies more than two orders of magnitude above the usually required values deemed acceptable for installation in the ultra high vacuum (UHV) of the main spectrometer and detector assembly [Wei23]. It is possibe that these initial outgassing rates can be reduced through adjusting the printer settings or the resin composition, baking the scintillator at a low temperature or by a prolonged exposure to vacuum.

4.3.2 Passive Layers

The scint-aTEF can be divided into three distinct surfaces which the electrons can encounter. These are the top of the scintillator grid, the sides of the scintillator grid (forming the inner channel walls) and the passive backplate.

The top of the scintillator grid does not discriminate between electrons with small and large angles. Instead, the ratio of electrons that hit the top surface is a fixed value given by the wall width and the total cell size. To enhance the angular discrimination of the scint-aTEF, it can be covered by a passive layer.

The inner walls of the square channels mostly absorb electrons with large angles (due to their large cyclotron radii). For an aTEF designed to primarily detect large angles while suppressing small ones, these sides must be "active". This is accomplished in the scint-aTEF by using a scintillator for the grid.

The backplate absorbs the remaining electrons, which have not been absorbed by the scintillator grid. Most of these transmitted electrons have low angles and are therefore not supposed to be detected by the aTEF. Thus, the back plate is made from a passive material, which absorbs the electrons without producing scintillation light. This layer also shields the SPAD-arrays from electrons.

The passive layer could consist of poly(methyl methacrylate) (PMMA) as mentioned in [Lau22] or a material similar to the resin used for the scintillator but without the scintillation components. Overall, the passive layer must have a similar optical refraction index as the scintillator to avoid internal reflections of scintillation photons between the scintillator grid and the passive backplate. The height of the passive layer must also be large enough to absorb the electron's energy, which amounts to $h_{\text{passive}} \gtrsim 10\,\mu\text{m}$ for 18.6 keV electrons [Gei22].

The structure is 3d printed directly onto the SPAD-array in order to ensure good optical coupling and increase structural stability

4.3.3 Single Photon Avalanche Diode Arrays

Single photon avalanche diodes (SPADs) are p-n-junctions operated in reverse bias mode above their breakthrough voltage, which creates a large electric field in the depletion layer. When a particle propagates through this layer and frees an electron, this electron will be accelerated by the electric field and free further electrons, triggering a self-sustaining avalanche of electrons. An electric circuit is used to read out and reset the SPAD-cell after an accumulation time. [ZTT+07], [CAG+21]

For the scint-aTEF, an array of SPAD-cells is used for event detection. The spacial resolution of the SPAD-array creates an "image" of the impact locations of the scintillation photons

when they hit the SPAD-array. Recent investigations using a SPAD-array ("IDP4") created at Heidelberg University [Sac16; Kel22], also mentioned in [Lau22], in combination with a ^{83m}Kr source with β-electrons in the keV range and a commercial plastic scintillator [Epi] have shown that the photon clusters produced by single electron events can be identified and distinguished from the background noise of the SPAD-cells [Sed23]. Event detection can be further improved by the use of advanced trigger groups as suggested in [Lau22] and a more advanced event detection algorithm, possibly involving a neural network. In addition, the post-acceleration electrode (PAE) of the KATRIN experiment could be used to increase the electron's energies by another 10 keV before they reach the aTEF to increase the amount of scintillation light (see section 6.7 for more information).

4.4 Angular Detection Efficiency for the scint-aTEF

When an electron encounters the scint-aTEF, its detection will depend on several parameters, which can be categorized into different groups: the experimental setup, the geometry of the scint-aTEF and the initial conditions of the particle.

The experimental setup includes the electron's kinetic energy E and the magnetic field strength B_{det} at the detector (i.e. the scint-aTEF).

The scint-aTEF geometry includes the height h_{scint} of the scintillator grid, the wall width d and the (total) cell width a_{cell} equal to the sum of the channel width and the wall width. Additionaly, a passive top layer of height h_{top} is included in the scint-aTEF geometry.

The initial conditions of the electron's trajectory include its position relative to the scintillator grid and its momentum direction given by an azimuthal angle φ_0 (initial phase) and the pitch angle θ. In the coordinate system used, the homogeneous magnetic field points in the negative z-direction. The electrons move in the positive z-direction towards the scint-aTEF. In this case, the pitch angle θ is defined as the angle between the electron's trajectory and the negative direction of the magnetic field lines such that electrons with angles $\theta < 90°$ move towards the detector.

The size of the cyclotron motion and the cell size of the scint-aTEF are much smaller than the beam size. Thus, the beam can be assumed to be homogeneous on the scale of a scint-aTEF cell. Furthermore, the initial phase φ_0 can be assumed to be evenly distributed in the interval $[0, 2\pi)$. The angular detection efficiency $\mathcal{E}(\theta)$ can be obtained by averaging over the initial position and phase:

$$\mathcal{E}(\theta) = \int \rho(x_0, y_0, \varphi_0)\, \mathcal{E}(\theta, x_0, y_0, \varphi_0)\, \mathrm{d}x_0\, \mathrm{d}y_0\, \mathrm{d}\varphi_0\,, \tag{4.1}$$

where $\mathcal{E}(\theta, x_0, y_0, \varphi_0)$ describes the angular detection efficiency for a given set of initial conditions (x_0, y_0, φ_0) and $\rho(x_0, y_0, \varphi_0)$ the probability density for these initial parameters. When neglecting electron backscattering at the scint-aTEF surface, the detection efficiency $\mathcal{E}(\theta, x_0, y_0, \varphi_0)$ for a single trajectory will either be 0 (not detected) or 1 (detected).

An electron's initial position can be described at an arbitrary location along its trajectory. For simplicity, a plane perpendicular to the magnetic field lines is chosen for the initial position of the electron trajectories. Moreover, this plane can be chosen to be directly in front of the scint-aTEF. Using the periodicity of the scint-aTEF, the possible initial positions can be reduced to the size of a single scint-aTEF cell.[2][3]

[2] In case of a tilted scint-aTEF (alignement errors), the plane of initial positions would have to be oriented with respect to the scint-aTEF (parallel to the backplate) instead of the magnetic field to achieve a periodic tiling of the beam.

[3] When using a simulation where the electron's initial position is not directly in front of the scint-aTEF, the beam tiling to restrict the initial positions to the size of a single scint-aTEF cell can still be used. However, multiple adjacent scint-aTEF cells will have to be simulated as electrons can now enter these nearby cells due to their cyclotron motion.

For a set of given initial conditions (transverse position x_0, y_0 and initial phase φ_0), a helical trajectory can be calculated using eq. (2.3) and (2.4) for the cyclotron radius and the height of the trajectory. When projecting this trajectory along the z coordinate, a circular segment is obtained, where the radius is equal to the cyclotron radius R_{cyc} and the phase advance (arc angle) $\Delta\varphi$ is given by the ratio of the scintillator height h_{scint} and the cyclotron height h_{cyc}:

$$\Delta\varphi = 2\pi \frac{h_{\mathrm{scint}}}{h_{\mathrm{cyc}}} \,. \tag{4.2}$$

The calculation of the average detection efficiency $\mathcal{E}(\theta)$ involves taking the integral over all initial variables x_0, y_0 and φ_0. This could be done using a Monte Carlo simulation to generate many different trajectories for randomized initial parameters. By running a subsequent check on how many of those trajectories intersect the scintillator grid, the detection efficiency for a fixed angle θ could then be obtained statistically.

Instead, another approach is pursued here, where the integral over the initial position x_0 and y_0 is replaced by geometrical considerations. This approach drastically reduces the computational effort necessary for the efficiency calculation of the scint-aTEF compared to the use of Monte Carlo Simulations (e.g. `Geant4`) as the angular efficiency $\mathcal{E}(\theta, \varphi_0)$ for a given initial phase can be calculated directly. The final integration

$$\mathcal{E}(\theta) = \frac{1}{2\pi} \int_0^{2\pi} \mathcal{E}(\theta, \varphi_0)\, \mathrm{d}\varphi_0 \tag{4.3}$$

can then be carried out numerically by averaging[4] over the efficiencies for $N \simeq 100$ evenly spaced initial phases according to

$$\mathcal{E}(\theta) \approx \frac{1}{N} \sum_{n=0}^{N-1} \mathcal{E}(\theta, \varphi_{0,n}) \,, \qquad \varphi_{0,n} = \frac{1}{2}\frac{1}{N}\frac{\pi}{2} + \frac{n}{N}\frac{\pi}{2} \,, \tag{4.4}$$

where the integral was reduced to the interval $[0, \frac{\pi}{2})$ due to the square symmetry of the scint-aTEF and the numerical integration is carried out using N bins of width $\frac{1}{N}\frac{\pi}{2}$.

The method to calculate the structural efficiency $\mathcal{E}_{\mathrm{grid}}(\theta, \varphi_0)$ for a square grid of height h, size a_{cell} and a wall width d is illustrated in figure 4.6. The structural efficiency herein refers to the probability of an electron hitting the grid structure. A rectangular bounding box with sides parallel to the inner channel walls of the grid is created around a trajectory for a given initial phase φ_0. If the bounding box is small enough, it can be "moved around" inside the square channel of the grid. The area traced by the initial position of the electron during this "movement" corresponds to the area A_{t} of possible starting locations for which the electron will be transmitted. It forms a rectangle where the side lengths correspond to the possible movement of the bounding box in the x- and y-direction without the electron being detected. The remaining area of the grid cell corresponds to initial locations for which the electrons will hit the grid structure. Thus, the angular efficiency for a given initial angle can be expressed as

$$\mathcal{E}_{\mathrm{grid}}(\theta, \varphi_0) = 1 - \frac{A_{\mathrm{t}}(\theta, \varphi_0)}{A_{\mathrm{cell}}} \,, \tag{4.5}$$

where $A_{\mathrm{cell}} = a_{\mathrm{cell}}^2$ is the area of a single cell of the grid structure.

For a scint-aTEF configuration without a top layer, the detection efficiency of the scintillator grid can be calculated directly via eq. (4.5). When using an additional passive top layer, eq. (4.5) can no longer be used directly to calculate the detection efficiency of the scintillator

[4] This is equal to the trapezoidal rule for a periodic function.

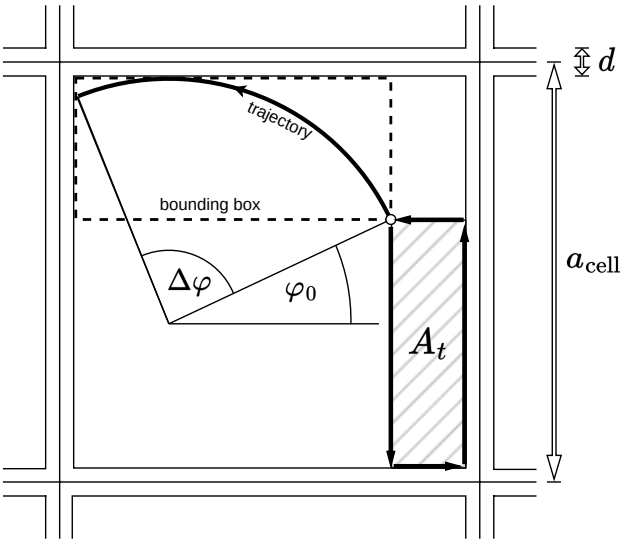

Figure 4.6: Angular efficiency calculation using geometric bounding boxes. The bounding box of the trajectory is created using lines parallel to the inner cell walls. Only electrons starting in the lower right area denoted by A will not be intercept the scintillator walls. All other electrons (corresponding to the remaining area of the cell) will reach the scintillator.

grid. This is because the detection efficiency of the scintillator grid now depends on the transmission characteristics of the passive top layer, which effectively acts as a pTEF with height h_{top}. This can be resolved by calculating the difference in the structural efficiency for two grid structures: one with the height of both the passive top layer and the scintillator grid and one with the height of the passive top layer only. The difference in structural efficiency between those two then yields the detection efficiency caused by the scintillator grid. This way ensures, that exactly those electrons are counted towards the scintillator grid, which are absorbed by the combined structure but not by the top layer. Using the linearity of eq. (4.3) the angular detection efficiency $\mathcal{E}(\theta)$ of the scint-aTEF with and without the top layer is then given by

$$\mathcal{E}(\theta) = \begin{cases} \mathcal{E}_{\text{grid}}(h_{\text{scint}}, \theta)\,, & \text{if top layer is removed} \\ \mathcal{E}_{\text{grid}}(h_{\text{scint}} + h_{\text{top}}, \theta) - \mathcal{E}_{\text{grid}}(h_{\text{top}}, \theta)\,, & \text{with passive top layer}\,. \end{cases} \tag{4.6}$$

Here, the dependence of $\mathcal{E}_{\text{grid}}(\theta)$ on the height h_{scint} and h_{top} has been explicitly written. The angular structural efficiencies $\mathcal{E}_{\text{grid}}(\theta)$ for the grid structures are averages of $\mathcal{E}_{\text{grid}}(\theta, \varphi_0)$, calculated according to equation (4.3) or (4.4). Figure 4.7 shows the angular efficiency of the scint-aTEF for different cell widths a_{cell}.

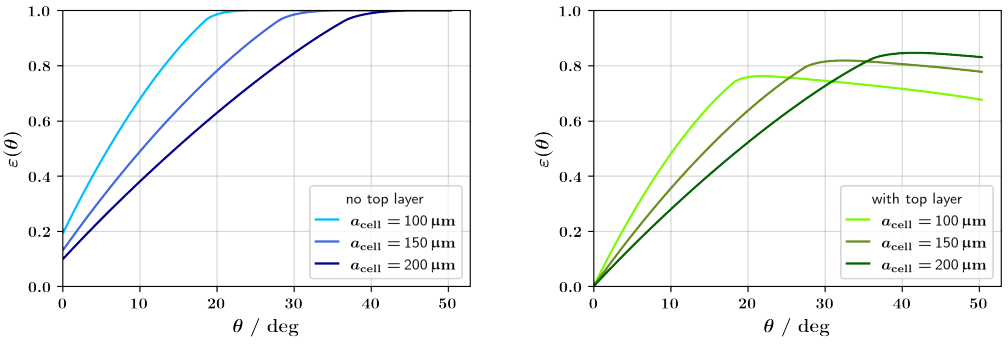

(a) active top

(b) top covered by a passive layer

Figure 4.7: Angular efficiency of the scint-aTEF for a cell width of 150 µm and $B = 2.4\,\mathrm{T}$. **(a)** Angular efficiency without a top layer. 100 % detection efficiency is reached above for large angles when electron backscattering is not included. **(b)** Angular efficiency for a scint-aTEF configuration with a passive top layer. The overall efficiency for both small and large angles is reduced. The slight decrease in efficiency for large angles is caused by the height of the passive layer, which essentially acts as a pTEF.

5. Simulation of the KATRIN Experiment

Determining the effect of the scint-aTEF on the KATRIN experiment requires a good understanding of how the KATRIN experiment responds to the β-spectrum and how the neutrino mass measurement is impacted by the scint-aTEF. For this, a simulation was written in the `Python` language to describe the experiment's response to the β-spectrum with and without the scint-aTEF.[1]

The `Python` programming language was chosen due to its ease of use when combined with Python libraries such as `numpy` [HMvdW+20], which allows operation on multidimensional arrays, enabling one to easily inspect data associated to a particular effect. Other libraries used include `scipy` [VGO+20] for more advanced functions and `matplotlib` [Hun07] for visualization of the data.

The goal of the simulation is to determine the statistical uncertainty on the squared neutrino mass m_ν^2 in a setting with and without the use of the scint-aTEF to draw a conclusion about its overall effectiveness i.e. reduction of the uncertainty on m_ν^2. For this, it is sufficient to simulate the most important effects of the KATRIN experiment with regard to the overall shape of the measured integral β-spectrum and its angular distribution.

In principle, the scint-aTEF could have been added to an already existing integral spectrum simulation such as KaFit/SSC within the KASPER framework, which is one of the tools used in the neutrino mass analysis at KATRIN [AAB+21] and is based on [KBD+19]. The benefit of such an approach would be a more detailed simulation of the experiment including multi-patch fits which are necessary for the shifted analyzing plane (SAP) introduced during the third neutrino mass campaign. These benefits would come at the cost of a more complicated code base to work with and less ability to quickly inspect data generated during calculations (`C++` loops vs `numpy` arrays). In addition to the gained flexibility of writing an own implementation in the `Python` language, this process also helped in gaining a better overall understanding of both the experiment and the design choices made in KaFit/SSC for spectrum simulation.

5.1 General Approach of the Simulation

The simulation uses a binned approach to calculate the measured integral β-spectrum. Binning is used for the energy distribution of the electrons before and after scattering in the source and for the angular distribution. The bin width used is approximately $\Delta E \simeq 0.1\,\mathrm{eV}$ (100x finer binning for spectrometer transmission) and $\Delta\theta \simeq 0.25°$. Multidimensional arrays are used to store the binned data, where each of the properties mentioned above (E_initial, E_final and θ) is assigned its own array dimension. Further array dimensions include the spectrometer set points qU_ret for the retarding potential used during the β-scans and the number n of times an electron has scattered in the source.

[1] The code for the simulation described in this chapter has been uploaded to `https://nuserv.uni-muenster.de:8443/nathanael.gutknecht/scint-atef`.

Table 5.1: Default simulation inputs and settings.

symbol	default value	description	comment
m_ν^2	$0\,\mathrm{eV}^2/c^4$	squared neutrino mass	fit parameter
E_0	18 573.7 eV	endpoint of β-spectrum	fit parameter
E	$\in [18\,533.7, 18\,575.7]$eV	simulated energy range	zero signal rate is used for $E > E_0 + 2\,\mathrm{eV}$
ΔE_sim	$\simeq 0.1\,\mathrm{eV}$	width of energy bins in simulation	$\simeq 0.001\,\mathrm{eV}$ for spectrometer transmission
θ	$\in [0, \theta_\mathrm{max}]$	simulated angles	
$\Delta\theta_\mathrm{sim}$	$\simeq 0.25°$	width of angle bins in simulation	
n	≤ 4	number of scatterings in the WGTS	
FSD	`FSD_KNM2_T2`	final state distribution	[FSD23]
qU_ret	$\in \{18534, ..., 18709\}\,\mathrm{eV}$	spectrometer set points	
B_src	2.52 T	magnetic field in WGTS	
B_ana	6.308 Gauss	magnetic field at analyzing plane	$1\,\mathrm{Gauss} = 10^{-4}\,\mathrm{T}$
B_pinch	4.239 T	magnetic field at pinch manget	
B_det	2.4 T	magnetic field at detector	used for angle at the detector
U_PAE	–0.0 kV	post acceleration voltage	
Φ_det	$151.55\,\mathrm{T{\cdot}cm}^2$	magnetic flux at detector	sum for 148 pixels, used for signal rate
N_px	117	number of active pixels	
ε_T	0.9865	isotopic tritium purity	
$\rho\mathrm{d}$	$4.23 \cdot 10^{17}\,\mathrm{cm}^{-2}$	column density	
σ_inel	$3.637 \cdot 10^{-18}\,\mathrm{cm}^2$	inelastic scattering crossection	
eloss	"eloss-function"	energy loss for inelastic scattering	binned version of [ABB+21]
A_sig	1.0	signal scaling factor	fit parameter
MTD	`MTD-KNM2-v0`	measurement time distribution	[MTD20]
t	694.27 h	total measurement time	in interval $qU_\mathrm{ret} \in [18534, 18709]\,\mathrm{eV}$
r_bkg	$0.22\,\mathrm{s}^{-1}$	background rate	sum for 117 pixels, fit parameter
E_bkg	qU_ret	background energy	assumed monoenergetic
p_Ryd	0.3	Rydberg fraction of background	
f_np	1.112	non-poissionian background factor	scales uncertainty on background rate

The settings for the simulation are chosen to match the second neutrino measurement campaign (KNM2), for which publicly available data exists [ABB+22a]. The use of KNM2 further allows the use a "uniform fit", which combines all selected pixels of the focal plane detector into one effective pixel, thereby simplifying the analysis. This is possible because KNM2 does not use a shifted analyzing plane, which introduces substantial radial dependencies and requires the use of a multi-patch fit [LBD+22]. For KNM2 the differences calculated by KaFit between a uniform and a ring-wise fit are small, with the uniform fit leading to a slightly larger uncertainty on the neutrino mass [KaF21]. For simplicity, no radial or pixel-wise dependencies are implemented in the simulation described here.

The following sections describe the simulated components as well as the steps necessary to generate an integral spectrum and obtain a neutrino mass sensitivity. Many aspects of the following sections in this chapter either closely follow or are inspired by the spectrum calculation described in [KBD+19] and it's implementation in KaFit/SSC. The default values for the simulation are listed in table 5.1.

5.2 β-Spectrum and Final State Distribution

The β-spectrum is simulated in the relativistic approximation as described in eq. (1.12).

It is extended according to [KBD+19, eq. (51)] to include the possibility of a negative squared neutrino mass. Wile the true squared neutrino mass must not be negative, statistical fluctuations in the count rate of the integral β-spectrum can lead to a best fit value of $m_\nu^2 < 0$, which is why the model must include those cases. From the likelihood of obtaining a certain measured (and possibly negative) best fit value for m_ν^2, a confidence interval for the true, positive value of the squared neutrino mass can be obtained [AAB+21].

For the final state distribution (FSD) a precalculated list with pairs of final state energies V_i for tritium molecules and probabilities P_i is used [FSD23]. It is shown in figure 5.2.

The initial angular distribution of the beta spectrum can be assumed to follow an isotropic distribution [KBD+19]. Expressed in spherical coordinates and after integrating over the

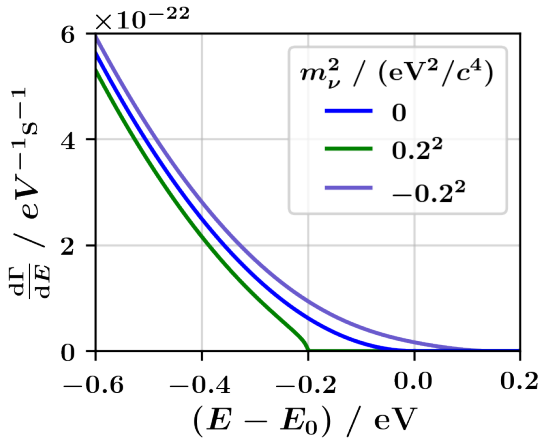

Figure 5.1: Extension of the β-spectrum to include the possibility of a negative squared neutrino mass.

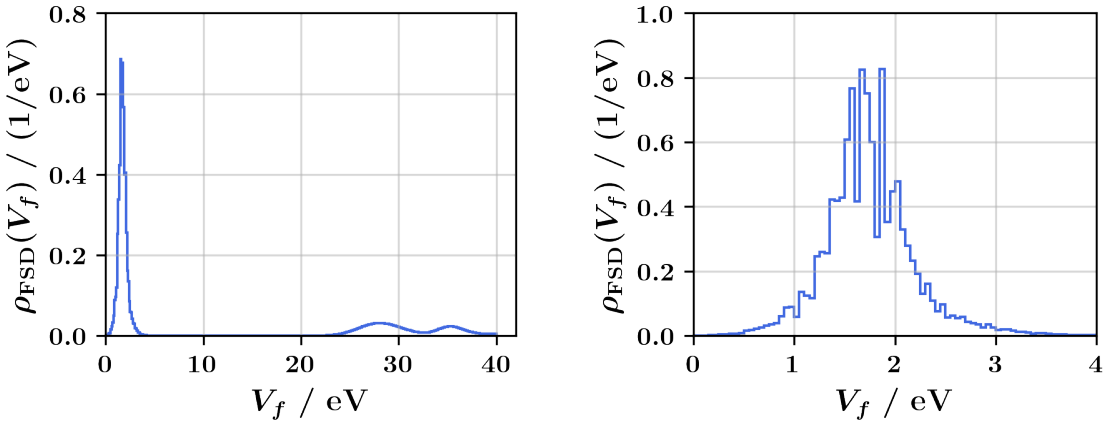

Figure 5.2: Final state distribution (FSD) for molecular tritium (T_2). **(a)** FSD shown as a probability density. **(b)** Zoomed- in version of (a).
Data from [FSD23].

azimuthal angle φ, this leads to an angular density of

$$\rho_\theta(\theta) = \frac{1}{2}\sin(\theta)\,, \tag{5.1}$$

meaning that larger angles occur more often than small angles (also see figure 4.2).

5.3 Inelastic Scattering within the Source and Associated Energy Loss

The large amount of tritium in the windowless gaseous tritium source (WGTS) means that some β-electrons will scatter with tritium molecules in the source. Only inelastic scattering is simulated as is is the dominant effect when comparing to elastic scattering [AAB+05]. During inelastic scattering the β-electrons lose some of their energy ($E_{\text{lost}} \geq 10\,\text{eV}$) while the angle θ is mostly left unchanged [KBD+19]. Scattering is simulated by first determining the probability $P_n(\theta)$ for n-fold scattering and then applying a distribution associated with the energy loss for n-fold scattering.

An electron starting at position z in the source will see an effective column density of

$$\rho_{\text{eff}}(z,\theta) = \frac{1}{\cos(\theta)}\int_z^{L/2}\rho(z')\,\mathrm{d}z'\,, \tag{5.2}$$

where $\rho(z)$ is the density of tritium molecules per volume in the source at position z and ρ_{eff} is a density of tritium molecules per area [KBD+19]. The term $1/\cos(\theta)$ describes the increased path length of an electron traveling at an angle θ through the source. The source exit is located at $z = L/2$. The probability for n-fold scattering depends on the initial position z and follows a Poisson distribution. It can be expressed as

$$P_n(\rho_{\text{eff}}(z,\theta)) = \frac{(\rho_{\text{eff}}(z,\theta)\cdot\sigma_{\text{inel}})^n}{n!} e^{-\rho_{\text{eff}}(z,\theta)\cdot\sigma_{\text{inel}}} = \text{Poisson}(\text{n}, \rho_{\text{eff}}(\text{z},\theta)\cdot\sigma_{\text{inel}})\,, \tag{5.3}$$

where σ_{inel} is the inelastic scattering cross section [KBD+19].

If no other location dependent effects are simulated (e.g. synchrotron radiation), the average scattering probability $P_n(\theta)$ can be calculated without knowing the density profile $\rho(z)$ by a substitution of the form

$$t = \frac{\rho_{\text{eff}}(z,\theta)}{\rho_{\text{eff}}(-\frac{L}{2},\theta)}\,, \tag{5.4}$$

where $\rho_{\text{eff}}(-\frac{L}{2},\theta)$ is the effective column density for electrons starting at the beginning of the source, located at $z = -\frac{L}{2}$. Using n-fold integration by parts, the average scattering probability $P_n(\theta)$ can be calculated to

$$\begin{aligned} P_n(\theta) &= \int_0^1 P_n\left(\frac{\rho\text{d}\cdot t}{\cos(\theta)}\right)\,\text{d}t \\ &= \frac{\cos(\theta)}{\rho\text{d}}\left(1 - \sum_{j=0}^{n}\text{Poisson}\left(\text{j}, \frac{\rho\text{d}}{\cos(\theta)}\right)\right)\,, \end{aligned} \tag{5.5}$$

where $\rho\text{d} = \rho_{\text{eff}}(-L/2, \theta{=}0)$ is the column density of the source. The resulting scattering probabilities are shown in figure 5.3.

The energy loss function is a probability distribution to describe the amount of energy lost in a single scattering. In this simulation, a pre-binned energy loss function from [ABB+21] is used. To describe the energy loss for n-fold scattering, the energy loss function must be convoluted with itself n times. Due to a minimum energy loss of 10 eV for each scattering and a decreasing probability for large numbers of scattering, it is sufficient to simulate the first few scatterings only. The energy loss functions for single and multiple scatterings are shown in figure 5.4.

5.4 Main Spectrometer Transmission and Pinch Magnet

The transmission condition for the main spectrometer is given in eq. (2.12) with $E_{\text{ana}} = E - qU_{\text{ret}}$. For energies $0 \lesssim E - qU_{\text{ret}} \lesssim \Delta E$ the transmission depends on both the energy E and the initial angle θ. For the simulation, the transmission condition is evaluated for each bin in energy and angle using the values at the bin center. The angular binning of the simulation automatically leads to a "detailed transmission", which respects the non-isotropic angular distribution of the β-electrons after scattering in the source.[2] To enhance the transmission calculation, each energy bin is subdivided into $\simeq 100$ equal-sized bins, for which the average transmission is calculated.[3]

The transmission condition for the pinch magnet is given by $\theta < \theta_{\text{max}}$, where the acceptance angle θ_{max} is given by eq. (2.9). By default, the angle bins are not extended beyond θ_{max} in the simulation for efficiency reasons. In such a case, the pinch magnet serves a redundant purpose.

[2] Due to the energy lost during scattering and the angular dependent scattering probability, electrons with the same energy at the source exit will no longer follow an isotropic angluar distribution.

[3] The default energy bins used in the simulation must cover the whole range of $-40\,\text{eV} \lesssim E - E_0 \lesssim 2\,\text{eV}$, which leads to a relatively coarse energy binning at the scale of the spectrometer resolution $\Delta E = 2.8\,\text{eV}$. This limitation arises from the use of arrays, which all share the same binning.

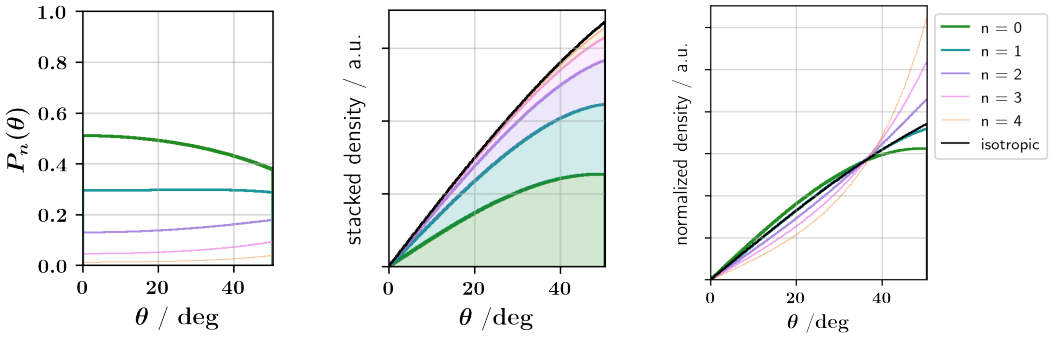

(a) **(b)** **(c)**

Figure 5.3: Scattering probabilities for $\rho d = 4.23 \cdot 10^{17}\,\mathrm{cm}^{-2}$. **(a)** Angular scattering probability. **(b)** Scattering probabilities applied to an isotropic distribution and stacked on top of each other. **(c)** Normalized angular distribution for n-fold scattering applied to an isotropic distribution. Note that these spectra have been scaled to better show the shape of the spectra.

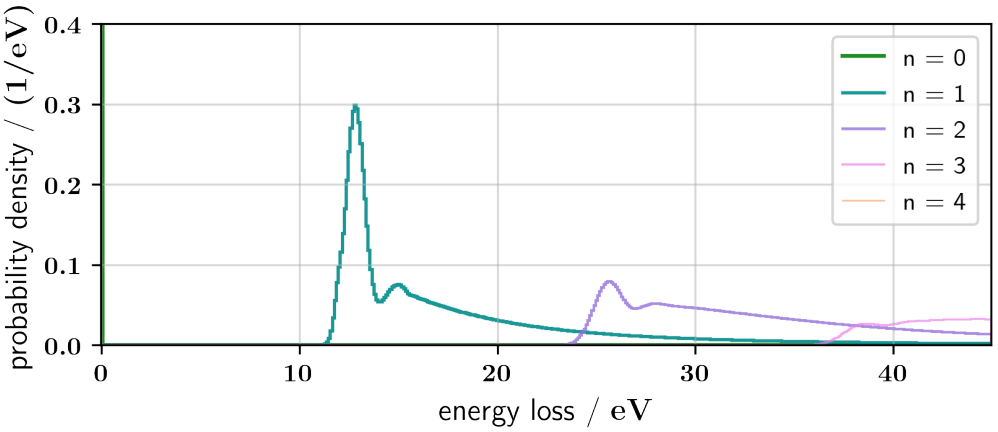

Figure 5.4: Energy loss functions used for n-fold scattering.

5.5 Detection Efficiency

Along the beamline, the energy and angle of the β-electrons has always been given with respect to the source potential and magnetic field. In the detector section, the energy of the electrons is increased by the post-acceleration electrode (PAE) to a kinetic energy of

$$E_{\mathrm{det}} = E - qU_{\mathrm{PAE}}\,. \tag{5.6}$$

The angle θ_{det} of the electrons at the detector is affected both by the magnetic field at the detector B_{det} and the energy increase qU_{PAE} by the post-acceleration electrode. Both of these affects are incorporated into the detector model, where B_{det} and qU_{PAE} are treated as detector properties.

These values for B_{det} and qU_{PAE} are used to calculate the new energy E_{det} and angle θ_{det} for each bin center using eq. (5.6) and (2.8). These values are then used to calculate the detection efficiency of the scint-aTEF according to eq. (4.6). This means that only the geometric detection efficiency of the scint-aTEF is used while further effects, such as electron backscattering or an internal detection efficiency of the scint-aTEF, are outside of the scope of this simulation.

As a reference, a second detector model is implemented to resemble the current focal plane detector (FPD). Due to the simple background model used (section 5.7), no advanced systems of the detector need to be modeled. The detection efficiency is set to 100 % as current simulations of the FPD show a detection efficiency of close to 100 % [ME23]. Furthermore, this allows for better comparability with the current implementation of the scint-aTEF.

5.6 Signal Rate

The signal rate is given by the β-decay spectrum (sec. 1.2) and the number of tritium molecules in the source. For the analysis, only 117 out of the 148 pixels of the FPD are used. The excluded pixels either have too much intrinsic noise or they do not receive the full count rate, meaning that parts of the beamline walls are mapped onto those pixels. [AAB$^+$21; ABB$^+$22a].

The total magnetic flux at the detector

$$\Phi_{\mathrm{det}} = B_{\mathrm{det}} A_{\mathrm{det}} \tag{5.7}$$

can be used to calculate the amount of tritium within the flux tube.[4] A_{det} is the area of the detector. The number of tritium atoms within the flux tube segment of the selected pixels can then be calculated to

$$N_T = \underbrace{2\varepsilon_T}_{\substack{\text{tritium atoms}\\ \text{per molecule}}} \cdot \underbrace{\rho \mathrm{d}}_{\substack{\text{column density}\\ \text{(number of}\\ \text{molecules}\\ \text{per area)}}} \cdot \underbrace{\frac{\Phi_{\mathrm{det}}}{B_{\mathrm{src}}}}_{\substack{\text{flux tube area}\\ \text{in WGTS}}} \cdot \underbrace{\frac{117}{148}}_{\substack{\text{fraction of}\\ \text{active pixels}}}\,, \tag{5.8}$$

where ε_T is the isotopic tritium purity [AAA$^+$19], given by the concentration of T_2, DT and HT in the source:

$$\varepsilon_T = \frac{c(\mathrm{T_2}) + 0.5(c(\mathrm{DT}) + c(\mathrm{HT}))}{c(\mathrm{T_2}) + c(\mathrm{DT}) + c(\mathrm{HT})}\,. \tag{5.9}$$

[4] This can only be applied to pixels receiving the full count rate.

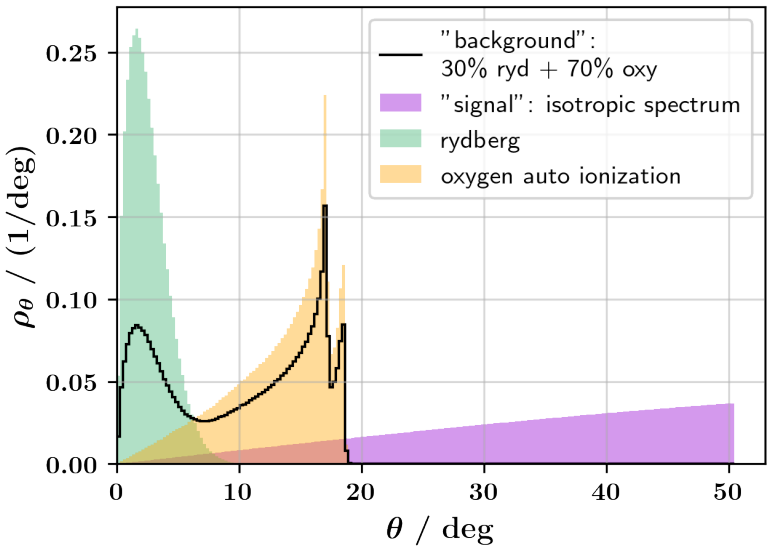

Figure 5.5: Angular distribution of the background as used in the simulation. The angular distribution is shown for $B_{\text{ana}} = 6.3\,\text{Gauss}$ and $B_{\text{src}} = 2.52\,\text{T}$. Only the first two peaks for oxygen autoionization are used. A composite distribution of 30 % Rydberg and 70 % oxygen autoionization background is shown as well as the initial isotropic distribution of the β-electrons.

5.7 Background

The components most likely making up large parts of the remaining background in KATRIN are the Rydberg (section 3.4) and oxygen autoionization background (section 3.5). These are included in the background model via their angular distribution at source potential and magnetic field. The energy distribution is approximated to be monoenergetic with an energy equal to the spectrometer setting qU_{ret}.

Data for the angular distribution is provided by D. Hinz from `Kassiopeia` simulations [FGT+17] for a normal (symmetric) analyzing plane with $B_{\text{ana, data}} = 5.0\,\text{Gauss}$ and $B_{\text{src, data}} = 2.5\,\text{T}$. This binned angular distribution is adjusted to the values of B_{ana} and B_{src} used in the simulation by applying eq. (2.8).[5] The transformed angular distributions are shown in figure 5.5.

A parameter $0 \leq p_{\text{ryd}} \leq 1$ describes the fraction of background rate attributed to the Rydberg background. Oxygen autoionization states are used for the remaining background fraction. A default value of 30 % Rydberg and 70 % oxygen autoionization background is used to account for the observations described in 3.5.

The measured background rate r_{bkg} must be manually set in the simulation. Because no radial dependencies of the background rate are simulated, the simulation is limited to scenarios where the flux tube is held at a fixed size i.e. B_{ana} is not changed.

[5] Here, the "initial" values of eq. (2.8) must be the desired values B_{ana} and B_{src} while the "final" values of eq. (2.8) are $B_{\text{ana, data}}$ and $B_{\text{src, data}}$ of the data provided. The transformation of the binned angular distribution is achieved by transforming the angles of the bin edges, followed by a rebinning process to match the predetermined bins of the simulation. During rebinning the content of the bins is assumed to be distributed homogeneously within each bin.

5.8 Experiment Response Function and Spectrum Calculation

The count rate $r_{\mathrm{sig}}(qU_{\mathrm{ret}})$ for the measured integral β-spectrum at qU_{ret} is given by

$$r_{\mathrm{sig}}(qU_{\mathrm{ret}}) = N_T \iiint \sum_n \frac{\mathrm{d}\Gamma}{\mathrm{d}E_i}(E_i)\ \rho_\theta(\theta)\ P_n(\theta)\ S_n(E_i - E_f) \\ T_{\mathrm{MS}}(qU_{\mathrm{ret}}, E_f, \theta)\ T_{\mathrm{pinch}}(\theta)\ \mathcal{E}(E_f, \theta)\,\mathrm{d}E_i\,\mathrm{d}E_f\,\mathrm{d}\theta\,, \tag{5.10}$$

where N_T is the number of tritium atoms, $\frac{\mathrm{d}\Gamma}{\mathrm{d}E_i}(E_i)$ is the differential β-decay spectrum, $\rho_\theta(\theta)$ is the angular distribution of the β-decay, $P_n(\theta)$ is the probability density in θ for n-fold scattering, $S_n(E_i - E_f)$ is the probability density for transitioning from an initial energy E_i to a final energy E_f (energy loss function) for n-fold scattering, $T(qU_{\mathrm{ret}}, E_f, \theta)$ is the transmission function of the main spectrometer for a setting of qU_{ret}, $T_{\mathrm{pinch}}(\theta)$ is the transmission function for the pinch magnet and $\mathcal{E}(E_f, \theta)$ is the detection efficiency of the detector.

The integrations over the energy after scattering E_f and the angle θ in eq. 5.10 can be carried out without knowing the shape of the differential β-decay spectrum. The count rate can then be written as

$$r_{\mathrm{sig}}(qU_{\mathrm{ret}}) = N_T \int \frac{\mathrm{d}\Gamma}{\mathrm{d}E_i}(E_i)\ R(qU_{\mathrm{ret}}, E_i)\,\mathrm{d}E_i\,, \tag{5.11}$$

where by doing this, the differential β-decay spectrum has been separated from the effects associated with the experiment[6]. These are now described by the experiment's response function

$$R(qU_{\mathrm{ret}}, E_i) = \iint \sum_n \rho_\theta(\theta)\ P_n(\theta)\ S_n(E_i - E_f)\ T_{\mathrm{MS}}(qU_{\mathrm{ret}}, E_f, \theta)\ T_{\mathrm{pinch}}(\theta)\ \mathcal{E}(E_f, \theta)\,\mathrm{d}E_f\,\mathrm{d}\theta\,. \tag{5.12}$$

The benefit of this approach is that it is sufficient to calculated the response function once for a certain configuration of the experiment. After that, it can be applied to various differential β-spectra[7] without the need to recompute all the effects of the experiment. The response function is shown in figure 5.6.

Another way to solve eq. (5.10) is to integrate over the initial energies E_i first to obtain the scattered differential spectrum at the source exit. The count rate is then described by

$$r_{\mathrm{sig}}(qU_{\mathrm{ret}}) = N_T \iint D(E_f, \theta)\ \tilde{R}(qU_{\mathrm{ret}}, E_f, \theta)\,\mathrm{d}E_f\,\mathrm{d}\theta\,, \tag{5.13}$$

where the scattered spectrum $D(E_f, \theta)$ is given by

$$D(E_f, \theta) = \rho_\theta(\theta) \sum_n P_n(\theta)\ \int \frac{\mathrm{d}\Gamma}{\mathrm{d}E_i}(E_i)\ S_n(E_i - E_f)\,\mathrm{d}E_i \tag{5.14}$$

and $\tilde{R}(qU_{\mathrm{ret}}, E_f, \theta)$ is a response function for just the rest of the experiment with

$$\tilde{R}(qU_{\mathrm{ret}}, E_f, \theta) = T_{\mathrm{MS}}(qU_{\mathrm{ret}}, E_f, \theta)\ T_{\mathrm{pinch}}(\theta)\ \mathcal{E}(E_f, \theta)\,. \tag{5.15}$$

The integral over the initial Energy E_i in eq. (5.14) describes a cross-correlation between the energy loss function for n-fold scattering and the differential β-decay rate. Such integrals can be efficiently calculated by algorithms, which make use of fast Fourier transform and the correlation theorem.

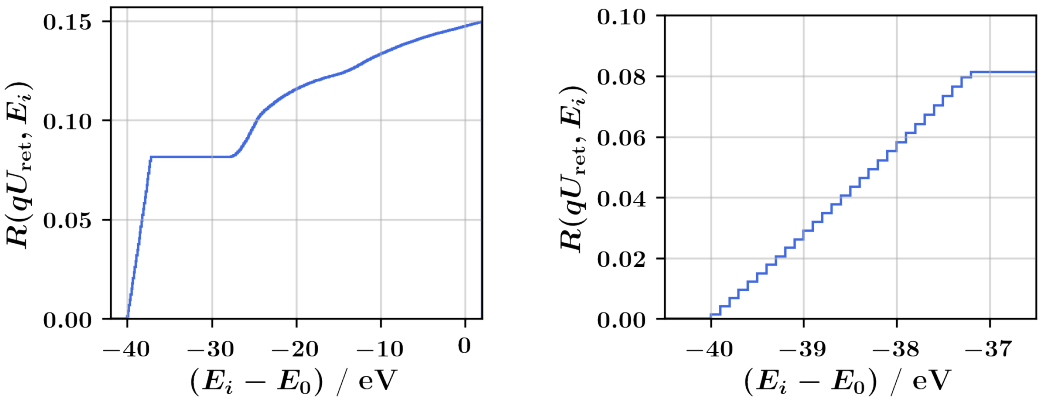

Figure 5.6: Response function of the experiment for $qU_{\mathrm{ret}} - E_0 = -40\,\mathrm{eV}$ (without the scint-aTEF). **(a)** The response function shows a plateau for $\Delta E < E - qU_{\mathrm{ret}} < 10\,\mathrm{eV}$. For surplus energies lower than the spectrometer resolution the spectrometer transmission depends on the angle. Electrons with a surplus energy of $E - qU_{\mathrm{ret}} > 10\,\mathrm{eV}$ can be transmitted even after scattering. **(b)** Zoomed version of (a).

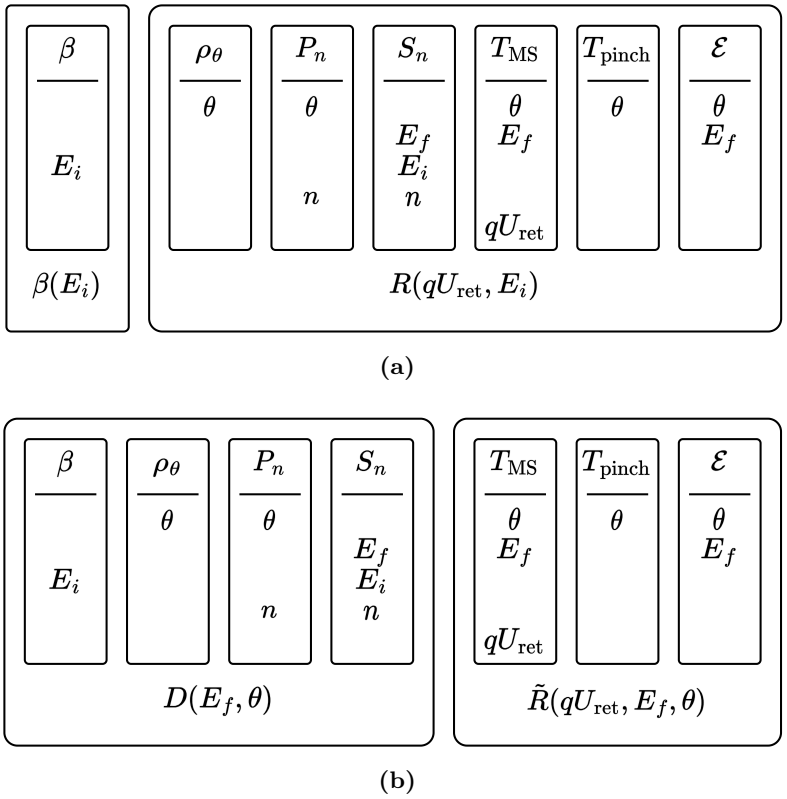

Figure 5.7: Simulation structure showing the different components and the array dimensions they act upon. Additional dimensions internal to a single component (e.g. sum over final states) are not shown. β: differential β-decay spectrum; ρ_θ: angular distribution (isotropic); P_n: probability for n-fold scattering; S_n: scattering matrix from initial to final energy for n-fold scattering; T_{MS}: transmission for the main spectrometer; T_{pinch}: transmission for the pinch magnet; $\mathcal{E}$: detector efficiency. **(a)** Calculating a response function $R(qU_{\mathrm{ret}}, E_i)$ groups all effects associated with the experiment together. **(b)** Different approach, where instead the scattered spectrum $D(E_f, \theta)$ is calculated. This requires recalculating the scattered spectrum for each new differential β-spectrum.

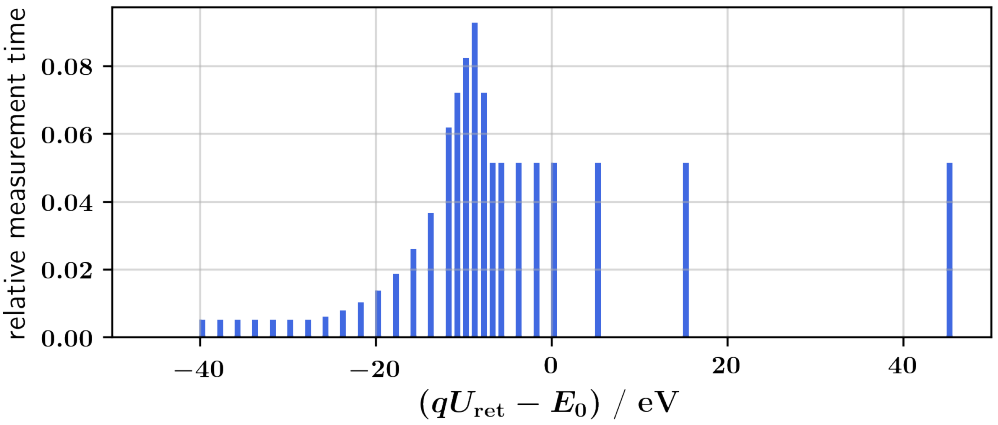

Figure 5.8: Measurement time distribution in the analysis window, given as a list of values for retarding energies qU_{ret} and relative measurement time t_{rel}. The last point at $qU_{\mathrm{ret}} - E_0 \approx 135\,\mathrm{eV}$ is outside of the shown area. Data from [MTD20].

Both approaches have been implemented; their structure is visualized in figure 5.7. It turns out that for this specific application the second approach of repeatedly calculating a scattered spectrum outperforms the approach of calculating a response function.[8]

5.9 Measurement Time Distribution

The measurement time distribution (MTD) describes the relative time spent at different retarding energies qU_{ret} when measuring the integral β-spectrum. For KNM2 this corresponds to a list with 28 values in the analysis interval between 18534 and 18709 eV,[9] corresponding to $E_0 - 40\,\mathrm{eV} \lesssim qU_{\mathrm{ret}} \lesssim E_0 + 135\,\mathrm{eV}$.

The input measurement time distribution for KNM2 is shown in figure 5.8. The qU_{ret} values beyond the endpoint are used to determine the background rate while the values deep in the spectrum are used to determine the signal rate and the location of the endpoint. Most of the time is spent in a region of a few electron volts below the endpoint, where the experiment is most sensitive to a neutrino mass.[Kle14]

In general, the measurement time distribution must be adjusted to both the statistical and the systematical uncertainties of the experiment. As the latter are not included here, no MTD optimization is performed.

5.10 Fit Procedure for Statistical Uncertainty on the Squared Neutrino Mass

In a neutrino mass fit, the shape of the integral β-spectrum near the endpoint is fitted. For this, the parameters for the squared neutrino mass m_ν^2, the endpoint E_0, a signal scaling

[6] As the angular distribution is not affected by the neutrino mass, the integration over θ is included in the experiment's response.

[7] e.g. corresponding to a different endpoint or neutrino mass.

[8] This is true for a typical scenario of a neutrino mass fit, where the scattered spectrum must be calculated multiple times compared to the response function, which is only calculated once. The reason for this difference in speed is the summation over large multidimensional response matrices necessary for obtaining the response function, where the combined effect of scattering and spectrometer transmission depends on four array dimensions (qU_{ret}, E_i, E_f and θ) simultaneously. In contrast, the second approach enables the summation over E_i before qU_{ret} and θ are introduced.

[9] Subsequent hardware scripts add 2 eV to this value to account for a potential depression of $\simeq -1.8\,\mathrm{eV}$. This means that the effective MTD for the β-electrons would be shifted by $\simeq 0.2\,\mathrm{eV}$ from the default MTD used here.

Table 5.2: Fit parameters obtained when fitting the described model on the KNM2 data as published in [ABB+22a, Source Data Fig. 2].

parameter	unit	best fit value
m_ν^2	eV^2/c^4	0.16 ± 0.31
E_0	eV	18573.68 ± 0.02
A_{sig}		0.986 ± 0.002
r_{bkg}	s^{-1}	0.2209 ± 0.0006

factor A_{sig} and the background rate r_{bkg} are estimated simultaneously using a χ^2-fit. The uncertainty on the squared neutrino mass $\sigma_{m_\nu^2}$ obtained from the fit is the sensitivity of the measurement.

The total rate measured is

$$r_{\mathrm{tot}}(qU_{\mathrm{ret}}) = r_{\mathrm{sig}}(qU_{\mathrm{ret}}) + r_{\mathrm{bkg}}. \tag{5.16}$$

The uncertainty on the count rate for a measurement point $_m$ at a retarding energy $qU_{\mathrm{ret},m}$ depends on the total measurement time t_m spent at that retarding potential and is given by

$$\sigma_{m,\mathrm{stat}} = \frac{\sqrt{r_m + f_{\mathrm{np}}^2 \cdot r_{\mathrm{bkg}}}}{\sqrt{t_m}}\,, \tag{5.17}$$

where Gaussian errors are used and f_{np} is a factor, which scales the uncertainty on the background rate, as it is wider than the expected Poisson distribution.

For the neutrino mass fit, a spectrum is generated with the default parameters given in table 5.1. A χ^2 minimization is performed using the function `scipy.optimize.curve_fit` with the minimization routine `method='trf'` (trust region reflective) and the keyword `absolute_sigma=True` to prevent an automatic scaling of the uncertainties on the data points. The function returns the optimized parameters and a covariance matrix containing the squared uncertainties of the fit parameters on the diagonal.

5.11 Crosscheck: Integral KNM2 Spectrum

As a crosscheck, the published data for the integral β-spectrum obtained in KNM2 [ABB+22a, Source Data Fig. 2] is used to perform a uniform fit (i.e. all 117 selected pixels are combined into one) on the data with the model described above. The fit results are shown in figure 5.9 and table 5.2.

The uncertainty on m_ν^2 matches the combined value for statistical and non-Poissionian background contribution of $\approx 0.31\mathrm{eV}^2/c^4$ from [ABB+22a, Table 2, values are quadratically added under the square root]. The obtained signal amplitude A_{sig} is a little low, but within 1 % of the value[10] from KaFit [KaF21].

The best fit value for m_ν^2 differs a lot from the value obtained in [ABB+22a]. This is due to some neglected effects such as the Doppler broadening caused by the motion of the tritium gas in the source. This effect distorts the β-spectrum in a similar way to a neutrino mass and must therefore be included when aiming for the correct neutrino mass [Kle14]. As the relative distortions on the combined signal and background spectrum are small, these effects don not influence the statistical sensitivity and therefore need not be included here.

[10] When using adjusted flux tube calculation [Beh22] and scaling the detection efficiency to 100 % for comparability.

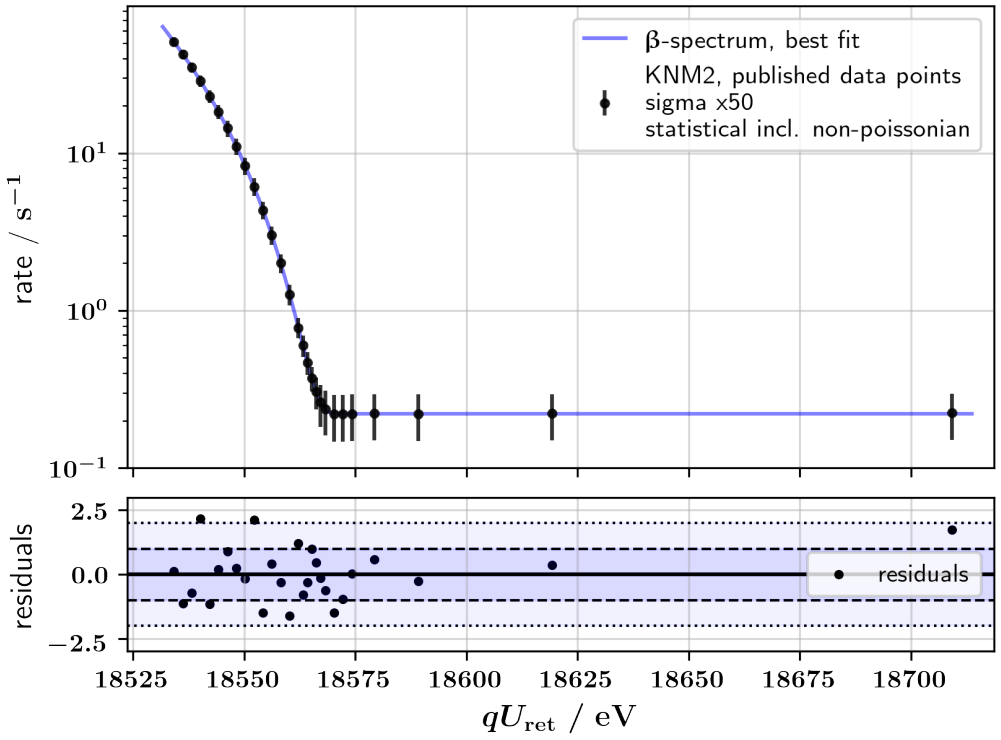

Figure 5.9: Uniform fit on KNM2 data published in [ABB+22a, Source Data Fig. 2].

6. Efficiency of the scint-aTEF and Impact on the Neutrino Mass Sensitivity of KATRIN

Within this chapter the results of the sensitivity study are presented. In sections 6.1 - 6.7 the signal- and background detection efficiency of the scint-aTEF is defined and its dependence on various parameters investigated. Following a brief discussion of the definition and meaning of signal efficiency (section 6.8), a KNM2-scenario is simulated to determine the effectiveness of the scint-aTEF in improving the neutrino mass sensitivity of the KATRIN experiment (section 6.9).

Unless otherwise noted, the default values from table 4.1 and table 5.1 are used for the scint-aTEF geometry and the simulation. The angular detection efficiency is calculated as described in section 5.5.

6.1 Detection Efficiency

The signal and background efficiency is defined as

$$\begin{aligned} \mathcal{E}_{\mathrm{sig}} &= \int \rho_{\mathrm{sig}}(\theta)\mathcal{E}(\theta)\,\mathrm{d}\theta \\ \mathcal{E}_{\mathrm{bkg}} &= \int \rho_{\mathrm{bkg}}(\theta)\mathcal{E}(\theta)\,\mathrm{d}\theta\,, \end{aligned} \tag{6.1}$$

where $\rho_{\mathrm{sig}}(\theta)$ is an isotropic angular distribution up to an angle θ_{max} for the electrons from β-decay and $\rho_{\mathrm{bkg}}(\theta)$ is the angular distribution of the background electrons, given by a composite spectrum of 30 % Rydberg electrons and 70 % from oxygen autoionization (figure 5.5). $\mathcal{E}(\theta)$ is the angular efficiency given by eq. (4.6) at the endpoint energy. The signal and background efficiency describe the average detection efficiency of the scint-aTEF for electrons following their respective angular distribution.

The cell width of the scint-aTEF determines the grid size of the scintillator, which detects electrons based on their cyclotron radii. Therefore, it has a large impact on the overall detection efficiency of both signal and background electrons. For a given cell width a_{cell} the signal and background efficiency can be calculated using eq. (6.1). By varying the cell width, different pairs of $(\mathcal{E}_{\mathrm{sig}}, \mathcal{E}_{\mathrm{bkg}})$ can be obtained as shown in figure 6.1.

6.2 Dependence on Scintillator Height

By varying the cell width continuously from small to large sizes, a line can be traced in the efficiency plot, showing all the possible combinations for signal- and background efficiencies when keeping the cell width adjustable, i.e. it can be optimized for the specific application. Tracing such contours for different heights h_{scint} of the scint-aTEF shows diminishing returns for heights above 300 µm. When the top layer is removed, no additional gain is found beyond a height of 200 µm. Above this height, any effects caused by changes in height can be absorbed into the cell width of the scint-aTEF.

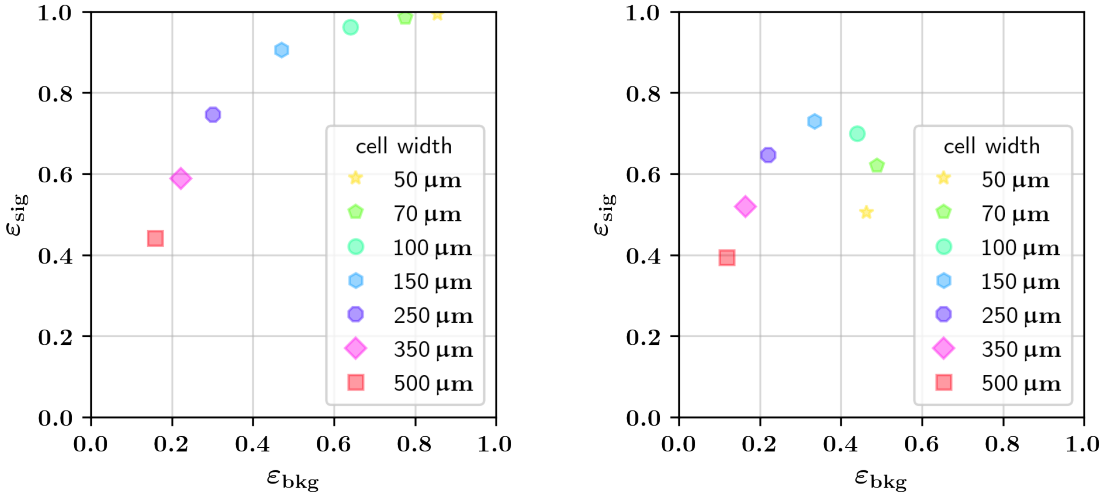

(a) without top layer **(b)** with passive top layer

Figure 6.1: Efficiency chart for the scint-aTEF. For the signal efficiency, an isotropic spectrum is used. The background is a composite spectrum of 30 % Rydberg and 70 % oxygen autoionization. **(a)** Scint-aTEF without a top layer. **(b)** Scint-aTEF with a passive top layer.

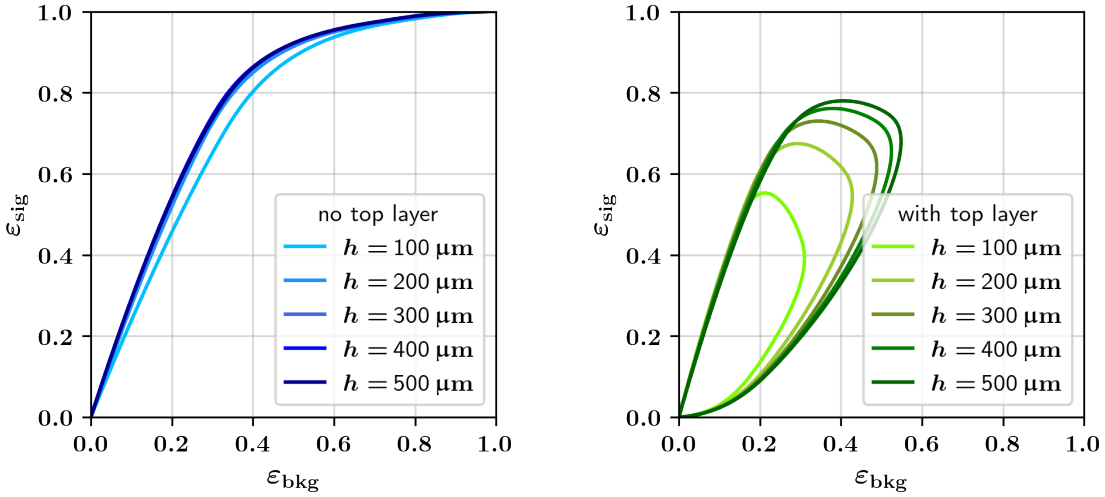

(a) without top layer **(b)** with passive top layer

Figure 6.2: Height dependence of the aTEF. The continuous lines are formed by varying the cell width for a constant height of the scintillator grid. **(a)** Scint-aTEF without a top layer. **(b)** Scint-aTEF with a passive top layer.

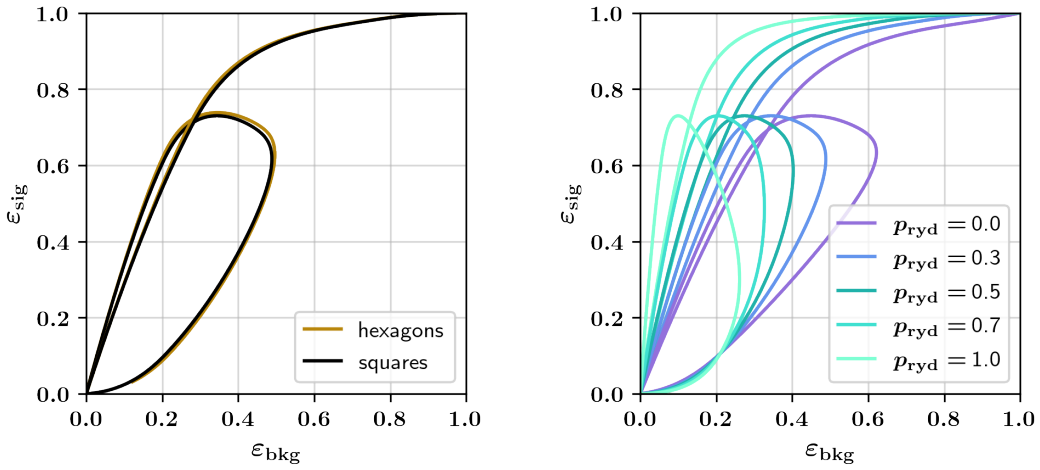

(a) **(b)**

Figure 6.3: **(a)** Efficiency achievable by the scint-aTEF when using different shapes. The same parameters are used for both the hexagons and the squares: scintillator height $h_{\text{scint}} = 300\,\mu\text{m}$, wall width $d = 10\,\mu\text{m}$, layer of top height $h_{\text{top}} = 10\,\mu\text{m}$, the cell width or edge length is variable. The two contours for the cases with ant without the top layer are shown in the same plot. The closed contour belongs to the scint-aTEF with a passive top layer while the other one describes the scint-aTEFR without the top layer. **(b)** The background efficiency depends on the background composition. The default composition assumes 30 % Rydberg electrons. See figure 5.5 for the angular distribution of the background components. Contours for the scint-aTEF with and without the passive top layer are shown, with the closed contours belonging to the scint-aTEF with a top layer.

6.3 Dependence on Shape

The scint-aTEF uses a square grid for the scintillator whereas other approaches use hexagonal channels [GSD+22]. To compare the effect caused by the shape, the algorithm described in section 4.4 to determine the geometric efficiency for a square grid is expanded to the shape of hexagons and cross checked with Monte Carlo simulations. Using the same values for grid height, wall width and top layer height for comparison, a similar behavior between the squares and hexagons can be observed with the hexagons performing slightly better (figure 6.3a). As the effect seems to be small, the shape of the scint-aTEF means that it can be chosen based on requirements for an optimal light transport in the scintillator.

6.4 Dependence on Background Composition

The background efficiency depends a lot on the fraction of Rydberg electrons in the background composition. This is shown in figure 6.3b. The oxygen autoionization background used here only contains initial energies $< 500\,\text{meV}$. Larger initial energies would lead to a lower fraction of the angular distribution below 20° [Lau22, Figure 5.4], which is where for typical cell widths the scint-aTEF actively discriminates based on the angle. By default, a fraction of 30 % Rydberg background is used (sec. 5.7).

6.5 Impact of the Passive Top Layer

From figure 6.3 it can be seen that the largest signal to background ratio can be achieved when using a passive layer to cover the top side of the scintillator grid. However, this comes at the cost of a lower signal efficiency, which is limited to less than 75 % when using the passive top layer. In the context of the KATRIN experiment and the current signal and

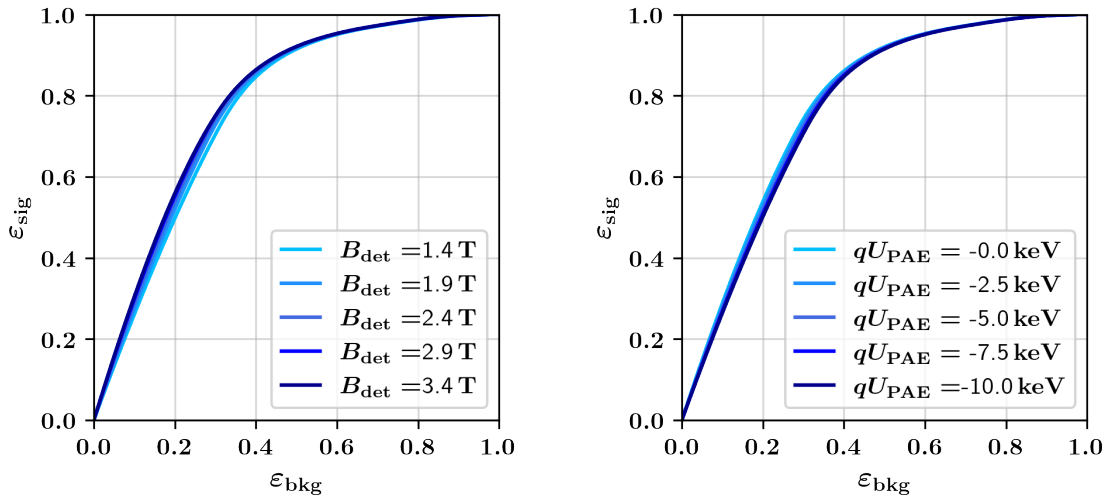

(a) **(b)**

Figure 6.4: **(a)** Scint-aTEF efficiencies for different magnetic fields at the detector. **(b)** Scint-aTEF efficiencies for different post-acceleration voltages.

background efficiencies, achieving a high signal efficiency is more important than optimizing the signal to background ratio.[1] Therefore, the passive top layer should be removed.

6.6 Dependence on the Magnetic Field at the Detector

Adjusting the magnetic field at the detector will change both angle and radius of the signal and background electrons. Figure 6.4a shows some, dependency on the magnetic field, though the effects seem small. One should note that B_{det} is assumed to be homogeneous and parallel to $\vec{e}_z$ in these calculations, which might not necessarily be the case. Furthermore, a good mapping of the flux tube onto the detector pixels is likely more important than the small gains from an increased field strength at the detector.

6.7 Impact of the Post-Acceleration Electrode

The post-acceleration electrode (PAE) will accelerate the electrons longitudinally, thereby increasing their cyclotron height and lowering their angle. As transverse momentum is conserved during longitudinal acceleration, the cyclotron radius of the electrons is left unchanged by the PAE. Figure 6.4b shows that the achievable detection efficiency does not drop much when using the PAE. This means that the PAE can be used for the scint-aTEF to increase the electron's energy and therefore the amount of scintillation light at the cost of increased backscattering. When the PAE is used, the height $h_{\mathrm{backplate}}$ of the passive backplate must be increased to 15 µm to account for the increased electron energy.

6.8 On Signal Efficiency and Scaling of the Response Function

The signal efficiency as defined in eq. (6.1), where $\rho_{\mathrm{sig}}(\theta)$ is an isotropic distribution, does not describe the ratio of the count rate at the detector with and without the scint-aTEF. This is shown in figure 6.5 and is due to the angular selection introduced both by inelastic scattering in the source and the spectrometer transmission.

The drastic reduction in relative count rate near the endpoint is of little concern. It can be viewed as an artifact, introduced by the angular dependent transmission characteristics of

[1] See section 6.9 for a direct comparison with regard to the neutrino mass sensitivity.

the main spectrometer (figure 6.6), which effectively shifts the measured endpoint of the integral β-spectrum for large angles (figure 6.7). The signal efficiency of the scint-aTEF should therefore not be thought of as a single number acting on a single β-spectrum but rather in terms of its angular dependent detection efficiency $\mathcal{E}(\theta)$, which acts on many different β-spectra, each one with its own amplitude and effective endpoint corresponding to a certain angle.

The question arises whether the signal efficiency $\mathcal{E}_{\text{sig}}$ used in section 6.1 through 6.7 is a good approximate description for the scint-aTEF. For this, $\mathcal{E}_{\text{sig}}$ is interpreted as a scaling factor for the initial isotropic angular distribution. Due to $E \approx E_0$ near the endpoint, the detection efficiency does not depend on the individual energy of the β-electron. Therefore, an effective angular distribution can be created[2] by combining the initial angular distribution with the angular detection efficiency of the scint-aTEF:

$$\rho_{\text{scint}-\text{aTEF}}(\theta) = \rho_{\text{sig}}(\theta)\,\mathcal{E}(\theta)\,. \tag{6.2}$$

In contrast, the angular distribution obtained from scaling the isotropic distribution is given by

$$\rho_{\text{scaled}}(\theta) = \rho_{\text{sig}}(\theta)\,\mathcal{E}_{\text{sig}}\,. \tag{6.3}$$

An example for both $\rho_{\text{scint}-\text{aTEF}}(\theta)$ and $\rho_{\text{scaled}}(\theta)$ is shown in figure 6.8a. Using the simulation described in chapter 5, it can be shown that adding or removing electrons from certain angle bins shows some angular dependent behavior (figure 6.8b).

Figure 6.9 shows the response function for both for the correct calculation and for the simplified approach using a scaled isotropic distribution. The scaling is done using the signal efficiency $\mathcal{E}_{\text{sig}}$ for an isotropic spectrum. The two response functions differ slightly in their heights. The most noticable difference between them is their different shape on the rising edge towards the first plateau.

The relative neutrino mass sensitivity obtained by these two response functions is shown in figure 6.10a. They both show a similar behavior. This is, however, due to chance and depends on the configuration of the experiment as shown in figure 6.10b. Furthermore, it can be seen from figure 6.10b that some settings can lead to a noticeable change in neutrino mass sensitivity despite showing similar values for signal and background efficiency. This means that the efficiency plots shown in sections 6.2 through 6.7 should be taken with caution. A better approach is to asses the change in neutrino mass sensitivity directly as it is done in the following section.

6.9 Impact on the Neutrino Mass Sensitivity

Using the full simulation described in chapter 5, the neutrino mass sensitivity for a KNM2-like scenario with a scint-aTEF is calculated. As before, the cell size is kept as an adjustable parameter. The sensitivity on the squared neutrino mass m_ν^2 with the scint-aTEF is then compared to the calculated case without the scint-aTEF. This process is repeated for different background compositions. The results are shown in figure 6.11.

For the assumed background composition of 30 % Rydberg and 70 % oxygen autoionization, a reduction factor of 12 % can be obtained by the scint-aTEF for a single neutrino mass campaign. This corresponds to a reduction in time of 22 % for reaching the same sensitivity as in the case without the scint-aTEF. Both values are given for a single campaign and do not include the time necessary for installing the scint-aTEF or taking data to study

[2] This new angular distribution must then be treated with 100 % detection efficiency as it already includes the detector effects.

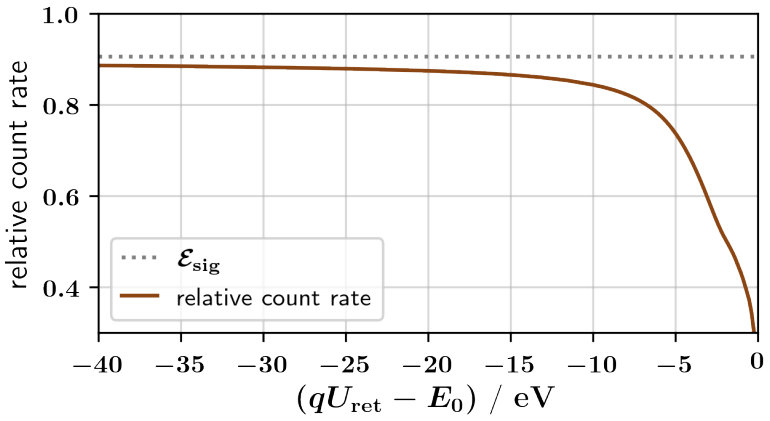

Figure 6.5: Relative count rate for signal electrons when using the scint-aTEF compared to the FPD. For reference the signal efficiency using an isotropic spectrum is shown. Over the whole integral spectrum the count rate is lower than the efficiency for an isotropic distribution. This effect is caused by angular selection due to scattering in the source. Near the endpoint the relative count rate drops significantly as here the angular selection of the spectrometer has the most impact.

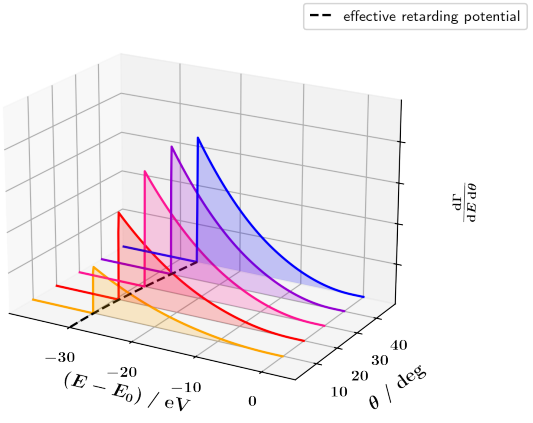

Figure 6.6: Differential β-decay spectrum after spectrometer transmission for $qU_{\mathrm{ret}} - E_0 = -30\,\mathrm{eV}$. Electrons with large angles require a higher total energy to be transmitted by the spectrometer. The maximum difference is given by the spectrometer resolution $\Delta E = 2.8\,\mathrm{eV}$.

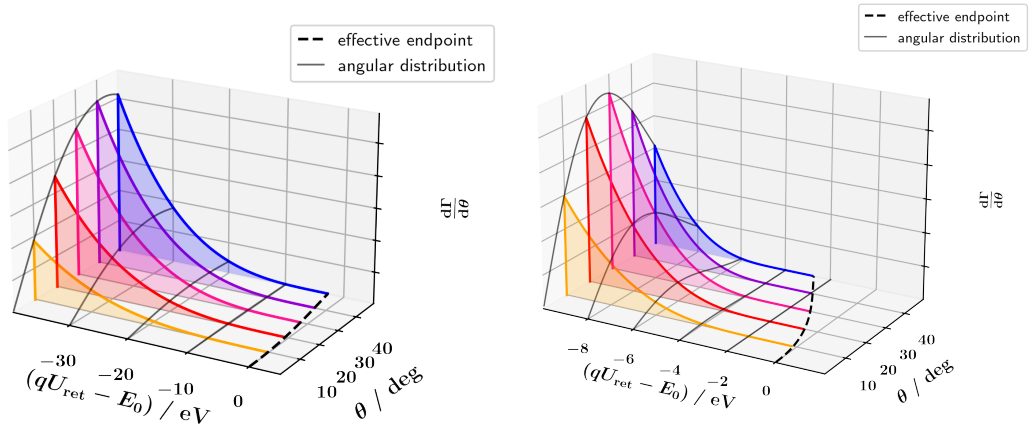

(a) **(b)**

Figure 6.7: Angular density of the integral β-spectrum. The main spectrometer causes an effective shift of the integral β-spectrum for large angles. The maximum shift is given by the spectrometer resolution of $\Delta E = 2.8\,\mathrm{eV}$. **(a)** Integral spectrum. **(b)** Zoomed version of (a).

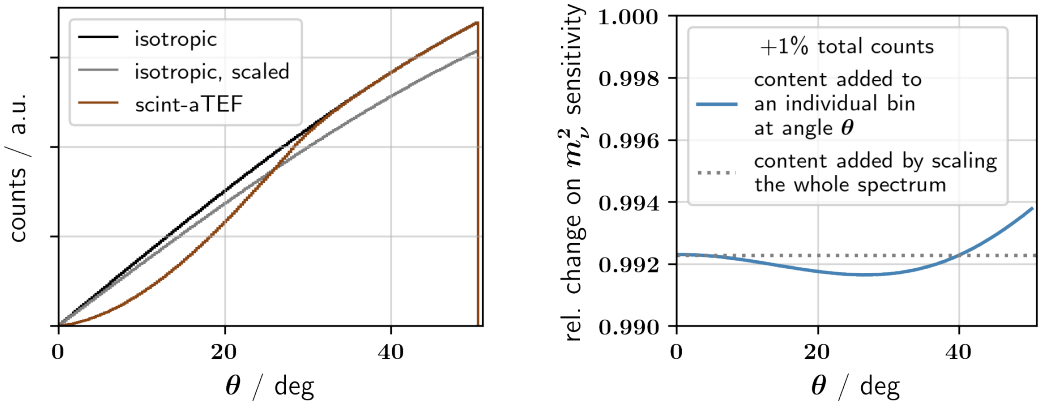

(a) **(b)**

Figure 6.8: Impact of angular distribution on the neutrino mass sensitivity. **(a)** The effective angular distribution $\rho_{\mathrm{scint-aTEF}}(\theta)$ is shown alongside the initial and scaled isotropic distributions ($\rho_{\mathrm{sig}}(\theta)$ and $\rho_{\mathrm{scaled}}(\theta)$). **(b)** 1 % of the total bin content is added to the initial isotropic spectrum, either in a single angle bin or by scaling the whole isotropic spectrum instead. Adding electrons with large angles is less effective than adding small or medium angles due to the increased scattering probability for large angles.

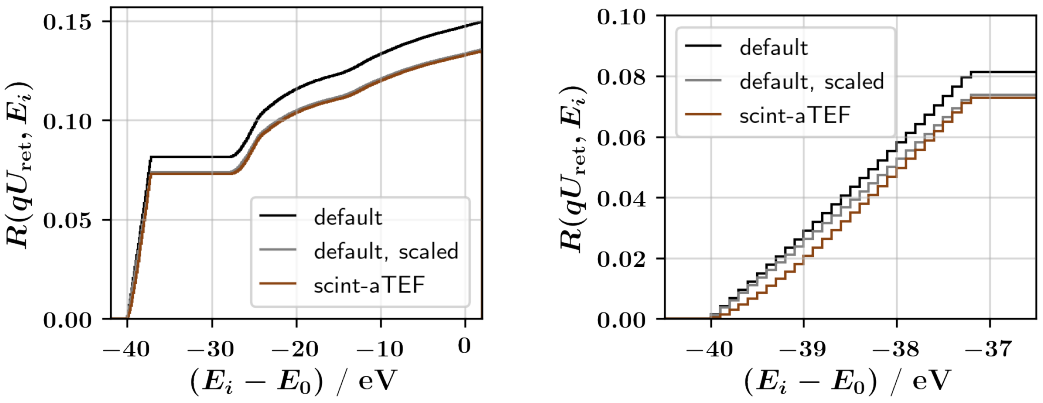

Figure 6.9: Response function for the scint-aTEF compared to the scaled response function for an isotropic angular distribution. **(a)** Response function. **(b)** Zoomed version of (a).

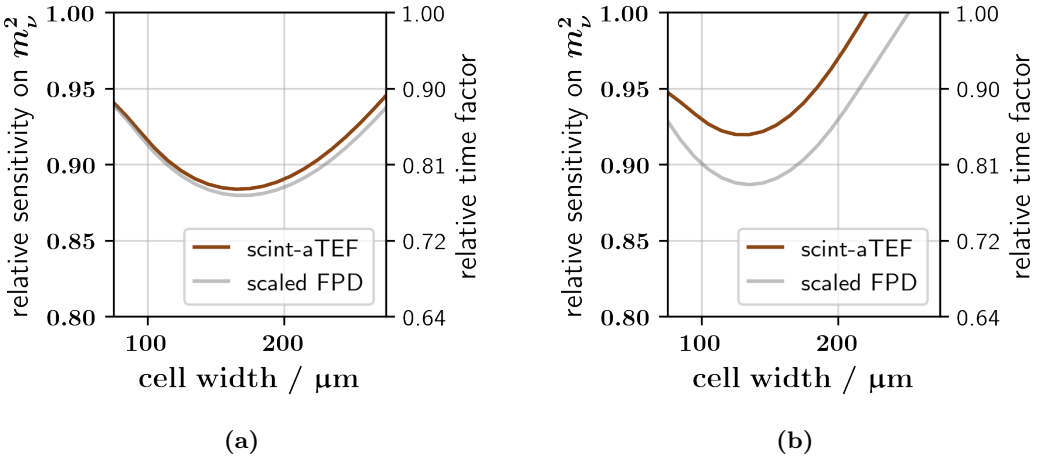

Figure 6.10: Relative neutrino mass sensitivity for the scint-aTEF, calculated with both the correct response function and the scaled isotropic one. For small cell sizes of the scint-aTEF the two approaches yield similar results. For large cell sizes the effect of the scint-aTEF is overestimated when using a scaled response function. **(a)** Default configuration of the scint-aTEF. **(b)** Same as (a), but with $qU_{\mathrm{PAE}} = -10\,\mathrm{keV}$. Here, the difference between the two approaches is no longer small.

the systematic effects introduced by the scint-aTEF. The relative reduction applies to the statistical sensitivity only and does not depend on the duration of the campaign. The overall sensitivity of KATRIN will be improved less than the given amount as the scint-aTEF does not apply to the first measurement campaigns.

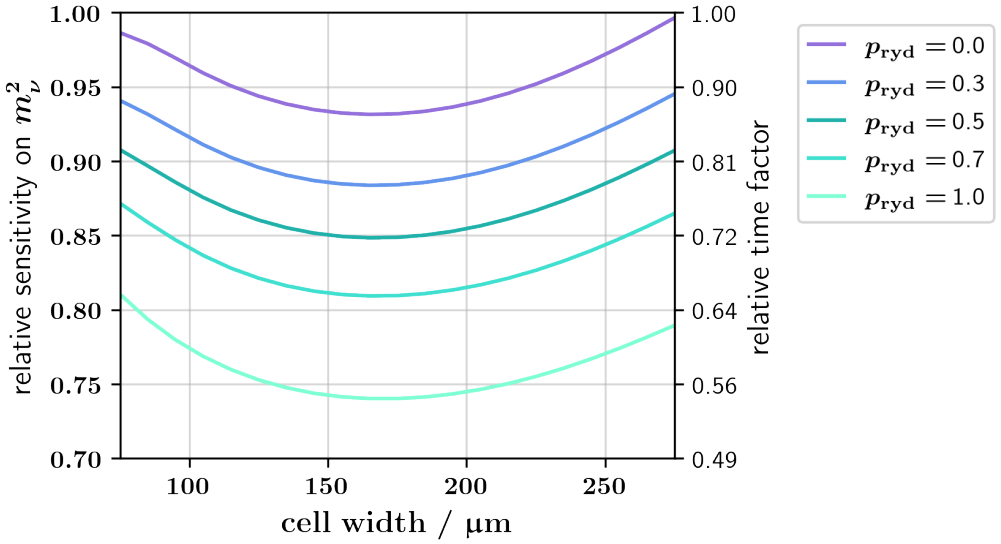

(a)

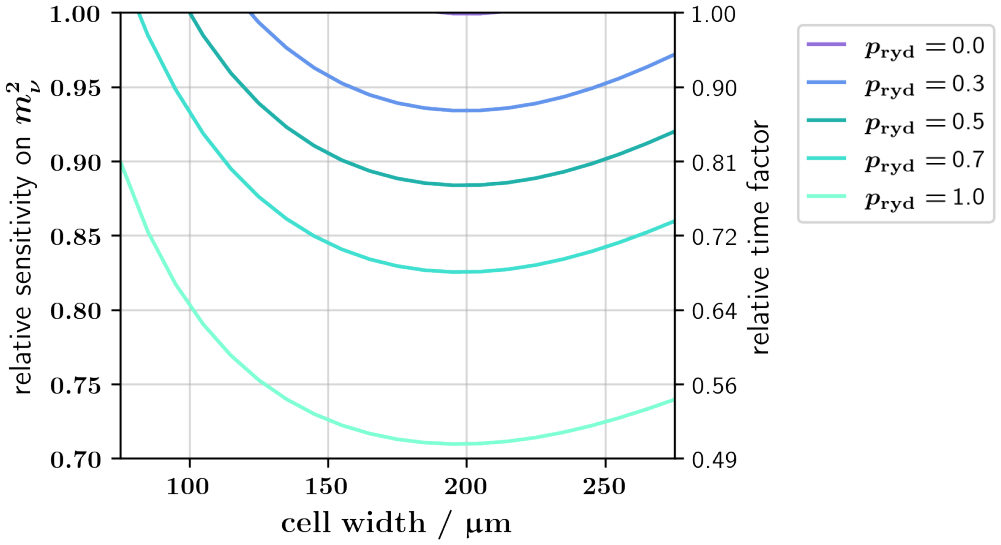

(b)

Figure 6.11: Relative sensitivity on m_ν^2 for a KNM2-like campaign when a scint-aTEF is used. The sensitivity improvement strongly depends on the background composition. **(a)** Scint-aTEF with the top layer removed. **(b)** Scint-aTEF with a passive top layer.

7. Conclusion

The scintillating active transverse energy filter (scint-aTEF) offers the potential to improve the neutrino mass sensitivity at KATRIN. This is achieved by a reduced detection efficiency for small angles, which are predominantly associated with background electrons. The angular discrimination and the achievable improvement in neutrino mass sensitivity depends on the geometry of the scint-aTEF as well as other setting of the experiment.

Using geometric considerations, an algorithm for calculating the geometric angular detection efficiency of the scint-aTEF was developed. This can be used to quickly test different scint-aTEF geometries for their detection capabilities regarding signal and background electrons.

Furthermore, a simulation of the main components of the KATRIN experiment was created, which uses binning for both energy and angle. From this simulation, a response function for the scint-aTEF is obtained.

It was discovered that the signal efficiency of the scint-aTEF, given as the detection efficiency for an isotropic spectrum, does not accurately describe the angular behavior of the scint-aTEF. Usign the signal efficiency to scale the response function for the FPD can lead to inaccurate estimations for the neutrino mass sensitivity.

Due to the overlap between the angular spectra of signal an background electrons and due to the statistical nature of the angular discrimination of the scint-aTEF, the background can only be reduced by simultaneously losing some of the signal electrons. Depending on the background composition, which is not fully known at the moment, this can severely limit the effectiveness of the scint-aTEF.

Using the simulation developed in the scope of this thesis, a KNM2-like scenario was simulated with and without the scint-aTEF. From this, it can be estimated that the scint-aTEF can reduce the statistical uncertainty on the squared neutrino mass within a campaign by approximately 12 % when assuming a background of 30 % Rydberg and 70 % oxygen autoionization electrons. The relative reduction does not depend on the duration of the campaign and corresponds to a reduction of 22 % in measurement time necessary to reach a predetermined neutrino mass sensitivity. The effect of the scint-aTEF is lessened, when it is introduced at a later stage of the experiment where part of the measurement has already been conducted without the scint-aTEF.

Bibliography

[AAA+03] S. Agostinelli et al. *"Geant4—a Simulation Toolkit"*. In: *Nuclear Instruments and Methods in Physics Research Section A: Accelerators, Spectrometers, Detectors and Associated Equipment* 506.3 (July 1, 2003), pp. 250–303. DOI: 10.1016/S0168-9002(03)01368-8.

[AAA+06] J. Allison et al. *"Geant4 Developments and Applications"*. In: *IEEE Transactions on Nuclear Science* 53.1 (Feb. 2006), pp. 270–278. DOI: 10.1109/TNS.2006.869826.

[AAA+16] J. Allison et al. *"Recent Developments in Geant4"*. In: *Nuclear Instruments and Methods in Physics Research Section A: Accelerators, Spectrometers, Detectors and Associated Equipment* 835 (Nov. 1, 2016), pp. 186–225. DOI: 10.1016/j.nima.2016.06.125.

[AAA+19] M. Aker et al. *"Improved Upper Limit on the Neutrino Mass from a Direct Kinematic Method by KATRIN"*. In: *Physical Review Letters* 123.22 (Nov. 25, 2019), p. 221802. DOI: 10.1103/PhysRevLett.123.221802.

[AAB+05] J. Angrik et al. *"KATRIN design report 2004"*. 2005. DOI: 10.5445/IR/270060419. preprint.

[AAB+21] M. Aker et al. *"Analysis Methods for the First KATRIN Neutrino-Mass Measurement"*. In: *Physical Review D* 104.1 (July 12, 2021), p. 012005. DOI: 10.1103/PhysRevD.104.012005.

[ABB+15] J. F. Amsbaugh et al. *"Focal-Plane Detector System for the KATRIN Experiment"*. In: *Nuclear Instruments and Methods in Physics Research Section A: Accelerators, Spectrometers, Detectors and Associated Equipment* 778 (Apr. 1, 2015), pp. 40–60. DOI: 10.1016/j.nima.2014.12.116.

[ABB+21] M. Aker et al. *"Precision Measurement of the Electron Energy-Loss Function in Tritium and Deuterium Gas for the KATRIN Experiment"*. In: *The European Physical Journal C* 81.7 (July 5, 2021), p. 579. DOI: 10.1140/epjc/s10052-021-09325-z.

[ABB+22a] M. Aker et al. *"Direct Neutrino-Mass Measurement with Sub-Electronvolt Sensitivity"*. In: *Nature Physics* 18.2 (2 Feb. 2022), pp. 160–166. DOI: 10.1038/s41567-021-01463-1.

[ABB+22b] M. Aker et al. *"KATRIN: Status and Prospects for the Neutrino Mass and Beyond"*. In: *Journal of Physics G: Nuclear and Particle Physics* 49.10 (Sept. 2022), p. 100501. DOI: 10.1088/1361-6471/ac834e.

[Beh22] J. Behrens. *"Flux Tube Calculation in SSC"*. KATRIN internal report. Feb. 15, 2022. URL: https://iap-katrin-wiki.iap.kit.edu/katrin/images/6/6d/AnaCall_20220214_FluxCalculationSSC.pdf (visited on 11/18/2023).

[BG15] S. M. Bilenky and C. Giunti. *"Neutrinoless Double-Beta Decay: A Probe of Physics beyond the Standard Model"*. In: *International Journal of Modern Physics A* 30 (04n05 Feb. 20, 2015), p. 1530001. DOI: 10.1142/S0217751X1530001X.

[CAG+21] F. Ceccarelli, G. Acconcia, A. Gulinatti, M. Ghioni, I. Rech, and R. Osellame. *"Recent Advances and Future Perspectives of Single-Photon Avalanche Diodes for Quantum Photonics Applications"*. In: *Advanced Quantum Technologies* 4.2 (2021), p. 2000102. DOI: 10.1002/qute.202000102.

[CRH+56] C. L. Cowan, F. Reines, F. B. Harrison, H. W. Kruse, and A. D. McGuire. *"Detection of the Free Neutrino: A Confirmation"*. In: *Science* 124.3212 (July 20, 1956), pp. 103–104. DOI: 10.1126/science.124.3212.103.

[Dyb19] S. Dyba. *"Background reduction by the inner wire electrode and set-up of the condensed krypton source at the neutrino mass experiment KATRIN"*. PhD thesis. 2019. URL: https://repositorium.uni-muenster.de/document/miami/4a73b204-96e6-4922-9d88-a640cd4ad191/diss_dyba.pdf.

[EBB+22] A. A. Esfahani et al. *"The Project 8 Neutrino Mass Experiment"*. Comment: contribution to Snowmass 2021. Mar. 14, 2022. DOI: 10.48550/arXiv.2203.07349. preprint.

[EBB+23] A. A. Esfahani et al. *"Tritium Beta Spectrum Measurement and Neutrino Mass Limit from Cyclotron Radiation Emission Spectroscopy"*. In: *Physical Review Letters* 131.10 (Sept. 6, 2023), p. 102502. DOI: 10.1103/PhysRevLett.131.102502.

[Epi] Epic-Crystal. *"Plastic Scintillator"*. URL: https://www.epic-crystal.com/data/upload/20230823/64e582d58cbbb.pdf (visited on 11/14/2023).

[FEE05] R. Feifel, J. H. D. Eland, and D. Edvardsson. *"Valence Double Ionization of O2 at Photon Energies below and above the Molecular Double Ionization Threshold"*. In: *The Journal of Chemical Physics* 122.14 (Apr. 11, 2005), p. 144308. DOI: 10.1063/1.1872836.

[Fer34] E. Fermi. *"Versuch einer Theorie der β-Strahlen. I"*. In: *Zeitschrift für Physik* 88.3 (Mar. 1, 1934), pp. 161–177. DOI: 10.1007/BF01351864.

[FGT+17] D. Furse et al. *"Kassiopeia: A Modern, Extensible C++ Particle Tracking Package"*. In: *New Journal of Physics* 19.5 (May 16, 2017), p. 053012. DOI: 10.1088/1367-2630/aa6950.

[Frä10] F. M. Fränkle. *"Background Investigations of the KATRIN Pre-Spectrometer"*. PhD thesis. 2010. DOI: 10.5445/IR/1000019392.

[Fra17] F. M. Fraenkle for the KATRIN collaboration. *"Background Processes in the KATRIN Main Spectrometer"*. In: *Journal of Physics: Conference Series* 888.1 (Sept. 2017), p. 012070. DOI: 10.1088/1742-6596/888/1/012070.

[FSB+22] F. M. Fränkle et al. *"KATRIN Background Due to Surface Radioimpurities"*. In: *Astroparticle Physics* 138 (May 1, 2022), p. 102686. DOI: 10.1016/j.astropartphys.2022.102686.

[FSD23] FSD_KNM2_T2.txt. internal file. Feb. 22, 2023. URL: https://nuserv.uni-muenster.de:8443/vsibille/KATRIN_FSD/-/blob/master/FSD_KNM2_T2.txt (visited on 11/16/2023).

[Gei22] T. Geigle. *"Geant4 Simulation Studies for Scintillating Transverse Energy Filters for KATRIN"*. unpublished. BA thesis. Karlsruhe Institute of Technology, May 2, 2022.

[GSD+22] K. Gauda et al. *"An Active Transverse Energy Filter to Differentiate Low Energy Particles with Large Pitch Angles in a Strong Magnetic Field"*. In: *The European Physical Journal C* 82.10 (Oct. 18, 2022), p. 922. DOI: 10.1140/epjc/s10052-022-10858-0.

[Hac17] M. T. Hackenjos. *"KATRIN "First Light" - Commissioning and Modelling of the Beamline"*. PhD thesis. 2017. DOI: 10.5445/IR/1000078933.

[Har15] F. T. Harms. *"Characterization and Minimization of Background Processes in the KATRIN Main Spectrometer"*. PhD thesis. 2015. DOI: 10.5445/IR/1000050027.

[Hin22] D. F. Hinz. *"Background systematics and extensions to the KATRIN background model"*. PhD thesis. 2022. DOI: 10.5445/IR/1000151022.

[HMvdW+20] C. R. Harris et al. *"Array Programming with NumPy"*. In: *Nature* 585.7825 (7825 Sept. 2020), pp. 357–362. DOI: 10.1038/s41586-020-2649-2.

[Hol07] J. Holdsworth. *"Čeština: Beta Rozpad Neutronu"*. Mar. 9, 2007. URL: https://commons.wikimedia.org/wiki/File:Beta_Negative_Decay.svg (visited on 11/05/2023).

[Hun07] J. D. Hunter. *"Matplotlib: A 2D Graphics Environment"*. In: *Computing in Science & Engineering* 9.3 (May 2007), pp. 90–95. DOI: 10.1109/MCSE.2007.55.

[Jac99] J. D. Jackson. *"Classical Electrodynamics (Third Edition)"*. 1999. URL: http://archive.org/details/john-david-jackson-classical-electrodynamics-wiley-1999 (visited on 11/07/2023).

[KaF21] KaFit Team. *"Final Unblinding Presentations - KaFit Results"*. internal document. Jan. 12, 2021. URL: https://iap-katrin-wiki.iap.kit.edu/katrin/images/f/f5/12-01-2021-KaFit-KNM2-unblinding-final.pdf.

[KBD+19] M. Kleesiek et al. *"β-Decay Spectrum, Response Function and Statistical Model for Neutrino Mass Measurements with the KATRIN Experiment"*. In: *The European Physical Journal C* 79.3 (Mar. 7, 2019), p. 204. DOI: 10.1140/epjc/s10052-019-6686-7.

[Kel22] M. Keller. *"Design and Low Temperature Characterization of Low Noise Single Photon Detector Arrays for Rare Event Search Experiments with Liquid Noble Gases"*. 2022. DOI: 10.11588/heidok.00032043.

[KKL+22] D. G. Kim, K. Kim, S. Lee, and Y. K. Kim. *"Enhanced Characteristics of 3D-Printed Plastic Scintillators Based on Bisphenol Fluorene Diacrylates"*. In: *Radiation Physics and Chemistry* 198 (Sept. 1, 2022), p. 110255. DOI: 10.1016/j.radphyschem.2022.110255.

[Kle14] M. Kleesiek. *"A Data-Analysis and Sensitivity-Optimization Framework for the KATRIN Experiment"*. PhD thesis. 2014. DOI: 10.5445/IR/1000043301.

[LAB+99] V. M. Lobashev et al. *"Direct Search for Mass of Neutrino and Anomaly in the Tritium Beta-Spectrum"*. In: *Physics Letters B* 460.1 (Aug. 5, 1999), pp. 227–235. DOI: 10.1016/S0370-2693(99)00781-9.

[Lau22] J. Lauer. *"Application Cases of Transverse Energy Filters in the KATRIN Experiment"*. Master thesis. 2022. URL: https://www.katrin.kit.edu/publikationen/mth_lauer.pdf.

[LBD+22] A. Lokhov et al. *"Background Reduction at the KATRIN Experiment by the Shifted Analysing Plane Configuration"*. In: *The European Physical Journal C* 82.3 (Mar. 26, 2022), p. 258. DOI: 10.1140/epjc/s10052-022-10220-4.

[ME23] A. Marsteller and S. Enomoto. *"Full FPD Simulation Based Update of Detector Systematics"*. 45th KATRIN Collaboration Meeting. Nov. 8, 2023. URL: https://indico.scc.kit.edu/event/3510/contributions/14814/ (visited on 11/16/2023).

[MHH+93] S. W. Moser, W. F. Harder, C. R. Hurlbut, and M. R. Kusner. *"Principles and Practice of Plastic Scintillator Design"*. In: *Radiation Physics and Chemistry* 41.1 (Jan. 1, 1993), pp. 31–36. DOI: 10.1016/0969-806X(93)90039-W.

[MNK97] S. Maruo, O. Nakamura, and S. Kawata. *"Three-Dimensional Microfabrication with Two-Photon-Absorbed Photopolymerization"*. In: *Optics Letters* 22.2 (Jan. 15, 1997), pp. 132–134. DOI: 10.1364/OL.22.000132.

[MTD20] MTD-KNM2-v0.dat. internal file. Feb. 28, 2020. URL: https://nuserv.uni-muenster.de:8443/katrin-git/kasper/-/blob/develop/KaFit/Data/MTD-KNM2-v0.dat (visited on 11/17/2023).

[MTW14] P. Mueller, M. Thiel, and M. Wegener. *"3D Direct Laser Writing Using a 405 Nm Diode Laser"*. In: *Optics Letters* 39.24 (Dec. 15, 2014), pp. 6847–6850. DOI: 10.1364/OL.39.006847.

[OW08] E. W. Otten and C. Weinheimer. *"Neutrino Mass Limit from Tritium β Decay"*. In: *Reports on Progress in Physics* 71.8 (July 2008), p. 086201. DOI: 10.1088/0034-4885/71/8/086201.

[Pau30] W. Pauli. *"Pauli Letter Collection: Letter to Lise Meitner"*. Letter. Typed copy. 1930. URL: https://cds.cern.ch/record/83282 (visited on 11/05/2023).

[PHM+20] F. Priester, D. Hillesheimer, A. Marsteller, M. Röllig, and M. Sturm. *"Tritium Processing Systems and First Tritium Operation of the KATRIN Experiment"*. In: *Fusion Science and Technology* 76.4 (May 18, 2020), pp. 600–604. DOI: 10.1080/15361055.2020.1730118.

[PYB+15] N. Palanque-Delabrouille et al. *"Neutrino Masses and Cosmology with Lyman-alpha Forest Power Spectrum"*. In: *Journal of Cosmology and Astroparticle Physics* 2015.11 (Nov. 2015), p. 011. DOI: 10.1088/1475-7516/2015/11/011.

[SAA+01] SNO Collaboration et al. *"Measurement of the Rate of $\nu_e + d \rightarrow p + p + e^-$ Interactions Produced by ^8B Solar Neutrinos at the Sudbury Neutrino Observatory"*. In: *Physical Review Letters* 87.7 (July 25, 2001), p. 071301. DOI: 10.1103/PhysRevLett.87.071301.

[Sac16] I. Sacco. *"Development of Highly Integrated PET/MR Detector Modules"*. 2016. DOI: 10.11588/heidok.00022239.

[Sch20] A. K. Schaller. *"Characterization and Mitigation of the Background in KATRIN"*. PhD thesis. Technische Universität München, 2020. URL: https://mediatum.ub.tum.de/?id=1553598 (visited on 10/25/2023).

[ŠDF08] F. Šimkovic, R. Dvornický, and A. Faessler. *"Exact Relativistic Tritium β-Decay Endpoint Spectrum in a Hadron Model"*. In: *Physical Review C* 77.5 (May 23, 2008), p. 055502. DOI: 10.1103/PhysRevC.77.055502.

[Sed23] Y. Seday. *"Single Event Reconstruction Techniques for Scintillating aTEFs"*. unpublished. BA thesis. Karlsruhe Institute of Technology, Aug. 20, 2023.

[SFH+98] Super-Kamiokande Collaboration et al. *"Evidence for Oscillation of Atmospheric Neutrinos"*. In: *Physical Review Letters* 81.8 (Aug. 24, 1998), pp. 1562–1567. DOI: 10.1103/PhysRevLett.81.1562.

[Sim81] J. J. Simpson. *"Measurement of the β-Energy Spectrum of ^{3}H to Determine the Antineutrino Mass"*. In: *Physical Review D* 23.3 (Feb. 1, 1981), pp. 649–662. DOI: 10.1103/PhysRevD.23.649.

[SKL+18] J. Son, D. G. Kim, S. Lee, J. Park, Y. Kim, T. Schaarschmidt, and Y. K. Kim. *"Improved 3D Printing Plastic Scintillator Fabrication"*. In: *Journal of the Korean Physical Society* 73.7 (Oct. 1, 2018), pp. 887–892. DOI: 10.3938/jkps.73.887.

[Tro19] N. R.-M. Trost. *"Modeling and measurement of Rydberg-State mediated Background at the KATRIN Main Spectrometer"*. PhD thesis. 2019. DOI: 10.5445/IR/1000090450.

[Val09] K. Valerius. *"Spectrometer-Related Background Processes and Their Suppression in the KATRIN Experiment"*. PhD thesis. 2009.

[VGO+20] P. Virtanen et al. *"SciPy 1.0: Fundamental Algorithms for Scientific Computing in Python"*. In: *Nature Methods* 17.3 (3 Mar. 2020), pp. 261–272. DOI: 10.1038/s41592-019-0686-2.

[WDB+99] Ch. Weinheimer, B. Degenddag, A. Bleile, J. Bonn, L. Bornschein, O. Kazachenko, A. Kovalik, and E. W. Otten. *"High Precision Measurement of the Tritium β Spectrum near Its Endpoint and Upper Limit on the Neutrino Mass"*. In: *Physics Letters B* 460.1 (Aug. 5, 1999), pp. 219–226. DOI: 10.1016/S0370-2693(99)00780-7.

[Wei23] S. Weis. *"Vacuum Compatibility Studies of Scintillating aTEF Detectors"*. unpublished. BA thesis. Karlsruhe Institute of Technology, 2023.

[Wor+22] R. L. Workman et al. *"Review of Particle Physics"*. In: *PTEP* 2022 (2022), p. 083C01. DOI: 10.1093/ptep/ptac097.

[ZTT+07] F. Zappa, S. Tisa, A. Tosi, and S. Cova. *"Principles and Features of Single-Photon Avalanche Diode Arrays"*. In: *Sensors and Actuators A: Physical* 140.1 (Oct. 1, 2007), pp. 103–112. DOI: 10.1016/j.sna.2007.06.021.